UC San Diego

UC San Diego Electronic Theses and Dissertations

Title

Investigation of cell environment interaction in vitro using a femtosecond laser

Permalink

https://escholarship.org/uc/item/47s8x5h1

Author

Zhang, Wande

Publication Date

2012

Peer reviewed|Thesis/dissertation

eScholarship.org Powered by the California Digital Library
University of California

UNIVERSITY OF CALIFORNIA, SAN DIEGO

Investigation of Cell Environment Interaction *In Vitro* Using a Femtosecond Laser

A dissertation submitted in partial satisfaction of the requirements for the degree Doctor of Philosophy

in

Bioengineering

by

Wande Zhang

Committee in charge:

Professor Shaochen Chen, Chair
Professor Marcos Intaglietta, Co-Chair
Professor Karen L. Christman
Professor Michael Heller
Professor Robert L. Sah

2012

Copyright

Wande Zhang, 2012

All rights reserved.

The dissertation of Wande Zhang is approved, and it is acceptable in quality and form for publication on microfilm and electronically:

_____

_____

_____

_____

Co-Chair

_____

Chair

University of California, San Diego

2012

DEDICATION

For my mother and grandparents

TABLE OF CONTENTS

Dedication iv
Table of Contents v
List of Figures viii
Acknowledgements x
Vita xiii
Abstract of The Dissertation xiv

CHAPTER ONE: Introduction 1

1.1 Investigation of cell-environment interaction 2

1.2 Investigating cell response by tuning the environment 4

1.2.1 Tuning topography at a micron-/nano-scale 4

1.2.2 Tuning the elasticity 6

1.2.3 Unique advantages of a femtosecond laser in environmental tuning 6

1.3 Investigating cell response through probing and manipulation of cells 8

1.3.1 Delivery of extracellular material into cells 8

1.3.2 Standardization of laser optoporation 9

1.4 Integrating the femtosecond laser fabrication with nanoimprinting 10

1.5 Scope of this dissertation 11

CHAPTER TWO: The femtosecond laser system 13

2.1 Introduction of the femtosecond laser 14

2.2 Mechanism of two phonton polymerization 14

2.3 Simulation of femtosecond laser ablation of cell membrane 17

2.4 Laser system setup 20
2.4.1 Optical system design 20
2.4.2 Design of the sample holder and adjust of its levelness 21
2.4.3 Automatic controlling system 22

CHAPTER THREE: Fabrication of negative Poisson's ratio structures and investigation of its influence on cell movement and division 27

3.1 Introduction 28

3.2 Materials and Methods 30
3.2.1 Preparation of polyethylene glycol diacrylate (PEGDA) 30
3.2.2 Preparation of sample substrate 31
3.2.3 Femtosecond laser fabrication of the webs 33
3.2.4 Femtosecond laser fabrication of fluorescence-labeled webs 35
3.2.5 Cells maintenance and seeding 35
3.2.6 Time-lapse imaging 36
3.2.7 Immunofluorescence labeling 36

3.3 Experiment design and results 38
3.3.1 NPR web design and fabricaiton 38
3.3.2 Cell experiment 39
3.3.3 Immunofluorescence staining results 42
3.3.4 Abnormal cell divisions 43

3.4 Conclusions 44

CHAPTER FOUR: Femtosecond laser-assisted optoporation for drug and gene delivery into single mammalian cells 52

4.1 Introduction 53

4.2 Materials and methods 56
4.2.1 Cell culture and preparation 56

4.2.2 Laser instrumentation set-up 56
4.2.3 Optoporation using femtosecond laser 58
4.3 Results and discussion 59
4.3.1 Cell survival with varying laser parameters 59
4.3.2 Optimization of laser conditions for cellular optoporation 60
4.3.3 Transfection of HEK cells by femtosecond laser-asisted cellular optoporation 62
4.4 Conclusions 63

CHAPTER FIVE: Integrated two-photon polymerization with nanoimprinting for direct digital nanomanufacturing 71
5.1 Introduction 72
5.2 Materials and methods 74
5.2.1 Material preparation for TPP 74
5.2.2 TPP fabrication process 76
5.2.3 Post-treatment of the mold 77
5.2.4 Imprinting in PEGDA 78
5.3 Results and discussion 80
5.4 Conclusions 82

CHAPTER SIX: Summary and future work 88
6.1 Summary 89
6.2 Future work 90
REFERENCES: 93

LIST OF FIGURES

Figure 2.1 SEM images of microdots array made of PEGDA hybrid material... 23
Figure 2.2 Distribution of normalized laser irradiance and free electron..... 24
Figure 2.3 Optical design of the femtosecond laser system. 25
Figure 2.4 Photos of the laser fabrication system..... 26

Figure 3.1 Schematic drawing of negative Poisson's ratio and positive Poisson's ratio..... 46
Figure 3.2 Bright field and fluorescent images of NPR and PPR webs 47
Figure 3.3 Schematic design of the femtosecond laser fabrication setup..... 48
Figure 3.4 NPR and PPR webs moved by cells..... 49
Figure 3.5 Immunofluorescence staining of 10T1/2 cells on NPR and PPR webs 50
Figure 3.6 Abnormal cell divisions on NPR webs in both bright field and fluorescent views 51

Figure 4.1 Schematic laser setup for optoporation 64
Figure 4.2 Bright field images of laser treated HEK cells: Trypan Blue (0.5%) was added to the culture medium 40 minutes after laser treatment to test cell-viability. Trypan Blue is a membrane-impermeable differential dye that stains dead cells but not live cells. 65
Figure 4.3 Bright field images (a, b, c) and fluorescence images (d,e,f) of intact HEK cells optoporation experiment in the presence of SYTOX dye. 66
Figure 4.4 Bright field (a,c) and fluorescence images (b,d) of an HEK cells after laser treatment in the presence of SYTOX dye..... 67
Figure 4.5 Morphological changes of two HEK cells (laser power = 60 mW; exposure time = 40ms) post-irradiation at the marked positions..... 68
Figure 4.6 Summary of femtosecond-optoporation results using HEK cell line 69
Figure 4.7 HEK cell transfection using femtosecond laser..... 70

Figure 5.1 Absorption spectra of DPPA with 1% photoinitiator and with 0% photoinitiator 84

Figure 5.2 Experimental setup of two-photon polymerization 85
Figure 5.3 Schematic diagram of the post-treatment of the mold surface 86
Figure 5.4 SEM images of the imprinted PEGDA structures and the DPPA mold after imprinting 87

ACKNOWLEDGEMENTS

PhD study was a long journey. I would not be able to get so much from it without the support and help from so many people.

First, I would like to thank my advisor Dr. Shaochen Chen for his support, guidance, and especially his encouragement and patience when I struggled for a long time to obtain scientifically significant results from my research. When I look back upon my PhD study, the most valuable thing I have obtained was a trained mind to ask the right questions, the ability to solve the problems, and the confidence to accomplish a complex project independently. Without the training and mentoring from Dr. Chen and the group he has established, I would not be what I am today.

I would also like to thank each of my committee members for being on my PhD committee and for their support throughout this process: Dr. Marcos Intaglietta, Dr. Robert Sah, Dr. Karen Christman, and Dr. Michael Heller. Specially, I would like to thank Dr. Intaglietta for being my co-advisor after I transferred to UCSD Bioengineering Department and mentoring me throughout the process of application, qualifying exam, senate exam, and defense.

I am deeply indebted to my mother and my grandparents for their love, support, and sacrifice. I do not think I will ever be able to pay them back in this life. So I dedicate this thesis to them, as the first step.

My work in this thesis would not have been possible without the contribution and help from the group members. I would like to thank Dr. Pranav Soman and Dr. Paul Qu for keeping feeding me with their crazy and fabulous research ideas. I would also like to thank Kyle Meggs for his help with the automation and optimization of the laser fabrication system, Sam Huang for helping me prepare methyacrylated slides, Peter Chung, Justin Liu, and John Warner for help with cell culture and biological equipment.

A number of former group members and fellow graduate students in UT Austin have helped me throughout my graduate study there. Particularly, I would like to acknowledge Dr. Li-Hsin Han for helping me build up my first experiment system. I would also like to thank Dr. Yi Lu, Dr. David Fozdar, and Dr. Arvind Battula for helping me get on my feet in the lab. Additionally, I would like to thank Dr. Jinze Qu, Dr. Sam Guo, and Dr. Junwei Wei for teaching me everything about laser optics and programming of controlling software.

Last but not least, I would like to acknowledge the National Science Foundation and the Office of Naval Research for providing grant to support my research.

The following chapters are, in part, reprints of the following publications:

Chapter 1 and Chapter 2, in part, is a reprint of material that is published as: Zhang W, Chen S. Femtosecond Laser Nanofabrication of Hydrogel Biomaterial. MRS Bulletin 2011; 36 (12): 1028-33

Chapter 3, in part, is in preparation for submission as: Zhang W, Soman P, Meggs K, Qu X, Chen S. Influence of Negative Poisson's Ratio on Cell Movement and Division

Chapter 4, in part, is a reprint of material that is published as: Soman P*, Zhang W*, Umeda A, Zhang Z, Chen S. Femtosecond Laser-Assisted Optoporation for Drug and Gene Delivery into Single Mammalian Cells. Journal of Biomedical Nanotechnology 2011; 7 (3): 334-41 *Shared first author

Chapter 5, in part, is a reprint of material that is published as: Zhang W, Han L-H, Chen S. Integrated Two-Photon Polymerization with Nanoimprinting for Direct Digital Nanomanufacturing. Journal of Manufacturing Science and Engineering 2010; 132 (3): 030907-5

VITA

Education:

September 2012	Ph.D., Bioengineering Department of Bioengineering University of California, San Diego
May 2009	M.S., Biomedical Engineering Department of Biomedical Engineering The University of Texas at Austin
July 2006	B.E., Mechanical Engineering Department of Mechanical Engineering University of Science and Technology of China

Publications:

Zhang W, Chen S. Femtosecond laser nanofabrication of hydrogel biomaterial. MRS Bulletin 2011; 36 (12): 1028-33

Soman P*, **Zhang W***, Umeda A, Zhang Zj,Chen S. Femtosecond Laser-Assisted Optoporation for Drug and Gene Delivery into Single Mammalian Cells. Journal of Biomedical Nanotechnology 2011; 7 (3): 334-41 *Shared first author

Suri S, Han L-H, **Zhang W**, Singh A, Chen S,Schmidt C. Solid freeform fabrication of designer scaffolds of hyaluronic acid for nerve tissue engineering. Biomedical Microdevices 2011; 13 (6): 983-93

Zhang W, Han L-H,Chen S. Integrated Two-Photon Polymerization With Nanoimprinting for Direct Digital Nanomanufacturing. Journal of Manufacturing Science and Engineering 2010; 132 (3): 030907-5

Fozdar Dy, **Zhang W**, Palard M, Patrick C,Chen S. Flash imprint lithography using a mask aligner: a method for printing nanostructures in photosensitive hydrogels. Nanotechnology 2008; 19 (21): 13

ABSTRACT OF THE DISSERTATION

Investigation of Cell Environment Interaction *In Vitro*

Using a Femtosecond Laser

By

Wande Zhang

Doctor of Philosophy in Bioengineering
University of California, San Diego, 2012

Professor Shaochen Chen, Chair
Professor Marcos Intaglietta, Co-Chair

The interaction between cells and their extracellular environment regulates diverse cell behavior such as migration, proliferation, and differentiation. At the tissue level, the cell-environment interaction determines the structure and organization of tissues and organs. Therefore, understanding of the cell-environment interaction provides the fundamental knowledge for the development of tissue engineering, biotechnology, and pharmaceutical research. Comparing to *in vivo* investigation of cell-environment interaction, *in vitro* study has attracted more interest because it allows users to analyze a

specific parameter independently in a controlled system. Two approaches have been followed by researchers to study cell-environment interactions. One approach is from the outside-in perspective, by tuning an environmental cue independently. The other approach is from the inside-out perspective, by probing and manipulating the cells. Much research progress has been made from both perspectives. However, the development of this area is still largely impeded by the inadequate capability to recapitulate the intricacy found in three-dimensional *in vivo* environment and to study a single cell. To provide fundamental insight into this field, new fabrication and manipulation tools must be developed to overcome those obstacles. A femtosecond laser, which has the capability to fabricate three-dimensional nanoscale structures and the ability to ablate a submicron hole in the cell membrane, is a promising candidate to further facilitate the research in this field. In this thesis, we used a femtosecond laser to tune the Poisson's ratio of the underlying substrate of cells, a fundamental property of materials. For the first time, suspended web structures exhibiting negative and positive Poisson's ratio were developed and the cell behavior on the web structures was analyzed. We also standardized the protocol for the femtosecond laser-assisted optoporation, which is widely used in the delivery of exogenous materials into cell interior to manipulate cellular activities. In addition, we combined the femtosecond laser fabrication with nanoimprinting to significantly increase the fabrication output for two-dimensional nanoscale structures.

CHAPTER ONE:

Introduction

1.1 Investigation of cell-environment interaction

The cell is the most fundamental unit of life which serves as the building block for every living organism. Most animal cells, except those which circulate in the blood, are anchorage-dependent and thus require attachment and interaction with extracellular environment to sustain their functional activities[1-3]. Loss of proper interaction with their environment can result in a cell entering apoptosis, or programmed cell death[4-6]. Therefore, understanding of the interaction between cells and their extracellular milieu, consisting of extracellular matrix (ECM) and dissolved molecules, is not only critical for basic cell biology research, but also a crucial factor in the development of tissue engineering, biotechnology, and pharmaceutical research[7, 8]. Recently, research efforts have focused in two categories of cell-environment interaction: *in vivo* and *in vitro* study. *In vivo*, Latin for "within a living organism" is the study of cells inside their natural environment—a living organism. *In vivo* research has the potential to allow a comprehensive study of a cell and all of its interactions with its environment. However, because the *in vivo* environment is an extraordinarily complex system containing a myriad of simultaneously occurring interactions and reactions, *in vivo* study lacks the capability to isolate specific factors and investigate them independently. Conversely, *In vitro* study, Latin for "within glass", is conducted in artificial environments and allows the user to simplify the system and isolate variables in order to conduct experiments in a controlled environment. Moreover, the *in vitro* research of a cell-environment is

of greater significance because of the *in vitro* system's wide utilization in biomedical applications. Therefore, in spite of still being a developing method, *in vivo* study has attracted an enormous amount of interest because of its unique versatility and programmability.

Two main approaches are largely being employed to study cell-environment interactions. One approach is from the outside-in. By tuning specific properties of the artificial ECM independently, one can analyze the subsequent cellular response. The other approach is from the inside-out. By probing and manipulating the cell membrane one can change cell behavior in a controlled environment. The research of the outside-in approach is developing rapidly as a result of the utilization of a variety of manufacturing tools which were initially used in semiconductor or rapid prototyping industries. Examples include: photolithography[9, 10], electron beam lithography[11, 12], soft lithography[13, 14], stereolithography[15, 16], and nanoimprinting[17, 18], which have been adopted to fabricate artificial biological structures. These methods have allowed researchers to create structures with different topographical, mechanical, chemical, and biological properties in order to mimic the multifold *in vivo* extracellular cues. The research from the inside-out has primarily focused on the delivery of exogenous genetic materials and/or drugs into cell interior to influence the intracellular activities. The exogenous materials are able to penetrate through the cell membrane with the assistance of various membrane-

poking tools, such as micro-injection[19, 20], gene gun[21, 22], electroporation[23, 24], and laser optoporation[25, 26].

Although there are a variety of fabrication and analysis tools available for the investigation of cell-environment interaction, the development of this area is still largely impeded by the obstacle of studying single cells in a replicated environment which matches the intricacy and detail found in three-dimensional *in vivo* environments. To provide fundamental insight into this field, new fabrication and manipulation tools must be developed in order to study single cells in an environment which resembles *in vivo* environments. In this thesis, I will demonstrate the potential of a femtosecond laser as a novel tool for both precise tuning of an environment as well as manipulating cells.

1.2 Investigating cell response by tuning the environment

1.2.1 Tuning topography at a micron-/nano-scale

Scientists have known for decades that cells respond to micro/nano-scale topographical and chemical cues in the ECM[27, 28]. In an artificial ECM, topographic patterning was fabricated by varying the shape and dimension of the patterns on a surface, while chemical patterning was generated by selectively positioning chemical cues such as growth factor or peptides on cell adhesion sites. Researchers have focused on developing various patterns to investigate the effects of micro/nano topographical and chemical patterns on

cell morphology[29-32], orientation, migration[33-37], stem cell differentiation[38-41], and tissue regeneration[42-44].

As all sorts of cell types and patterns were being investigated, it was hypothesized that a fundamental theory could be generalized about cell response to micro/nano-scale topography. However, this has not yet been proven and one interesting phenomenon remains in this field is that the results from different studies are occasionally contradictory. For instance, in one study, it was observed that polystyrene microgrooves shallower than 35 mirons were not able to guide fibroblast alignment[45]. In another study, researchers demonstrated that poly-L-lactide/trimethylene carbonate microgroove with the depth of 0.5 to 5 microns could guide the migration of myoblasts[46]. More evidence such as this has revealed that cell response to topography is not simply dependent on cell-type and material-type; it is dependent on the complex relationship of multiple factors. Therefore, there may not be a universal theory or mechanism which can be applied to every circumstance. Thus, for specific applications in health care or biological study, cell response on a specific structure will have to be examined case by case, requiring an accurate fabrication technique to produce arbitrary ECM patterns in order to mimic any *in vivo* situation.

1.2.2 Tuning the elasticity

It was discovered that the cells in different organs reside in different ECM with distinct elasticity, increasing from brain tissue, to muscle, to cartilage, and to bone[47, 48]. A cell is able to sense the elasticity of its environment by interacting with the substrate and, based on the reactionary force exerted on the substrate, generate unique signals through mechano-transducer molecules. The modification of the substrate elasticity has been observed to affect focal-adhesion structure[49, 50], cell migration[51], cell spreading[52], and stem cell differentiation[47, 53]. In order to change the elasticity of a structure, one may alter the biomaterial used, change its molecular weight, or simply change the cross-linking density during the polymerization process.

1.2.3 Unique advantages of a femtosecond laser in environmental tuning

A variety of novel methods have been developed and utilized to fabricate three-dimensional structures. Three-dimensional structures have a distinct advantage over two-dimensional ones, as they can mimic an *in vivo* environment more accurately. Those methods include, but are not limited to, solvent casting/salt leaching[54-56], gas foaming[57], electrospinning[58, 59], phase separation[60], solid freeform fabrication[61, 62], and membrane lamination[63]. Although these methods have been successfully applied in fabrication of an artificial ECM, they have not been demonstrated to provide an ideal control of ECM properties. Solvent casting/salt lamination, gas foaming, phase separation, and membrane lamination are capable of fabricating three-

dimensional structures, but relinquish precise control of size and shape of inner structures. Solid freeform fabrication is capable of fabricating three-dimensional structures with precise control of geometry, but because the fabrication resolution is limited to the range of tens to hundreds of microns, the resolution is too large to accurately mimic the *in vivo* submicron/nano-scale biological cues. In light of the rapid advancement in tissue engineering, researchers have searched for an alternative fabrication method which is capable of fabricating three-dimensional submicron/nano-scale structures with a high resolution and a precise control of geometry. Femtosecond laser induced two-photon polymerization is one promising technique which fulfills these requirements.

In chapter two of this thesis, I will explain the mechanism of femtosecond laser induced two-photon polymerization and demonstrate its fabrication capability. In chapter three, I will use a femtosecond laser to tune the Poisson's ratio of the underlying substrate of cells, a novel manipulation of a fundamental property of materials. This manipulation was previously prohibited by a lack of adequate fabrication tools, but made possible by femtosecond laser induced two-photon polymerization. I will use the femtosecond laser system to develop suspended web structures which exhibit negative and positive Poisson's ratio and analyze the cell behavior on the web structures.

1.3 Investigating cell response through probing and manipulation of cells

1.3.1 Delivery of extracellular material into cells

In today's biology and biotechnology studies, delivery of exogenous genetic materials, enzymes, or drugs through a cell membrane in order to monitor or influence cellular behavior is a practice with enormous potential to revolutionize the current research. One application is in the immunocytochemistry technique, which requires the delivery of reagents and antibodies into live cells. Another application is in drug test and gene transfection, where high throughput and cell viability are necessitated.

Exogenous materials are commonly delivered into cells through chemical delivery vehicles[64-66], viral vectors[67, 68], and physically penetrating methods such as electroporation[69] and the use of a gene gun. These methods allow manipulations and analyses of intact cells with high throughput. However, in most cases, cells are treated as a population and the resulting data only represents the average response of the entire population. Thus this technique is flawed, as it is well accepted that in certain biological applications, the cell-to-cell variability cannot be neglected. Therefore, because novel methods of single-cell manipulation and analyses provide detailed data previously unavailable through group analyses, scientists have begun to look towards other methods of extracellular material delivery.

Femtosecond laser assisted optoporation has been used to deliver extrinsic materials into a single cell with cell viabilities from 50% to 100% [70-77]. Cells stay intact during laser processing because the laser beam can produce a temporary submicron transient hole on the cell membrane which lasts only seconds before it heals itself. Therefore, because of its accuracy and precision, single cell manipulation using a femtosecond assisted optoporation technique could have far reaching effects in the field of bioengineering, tissue engineering and stem cell therapy [72].

1.3.2 Standardization of laser optoporation

In our study of femtosecond laser optoporation, we noted significant discrepancies in reported values for laser parameters[78-81]. This lack of consistency made the results obtained in one experiment not easily transplantable. The reason for the discrepancies was the lack of standardization, which is a major hurdle for the broader application of femtosecond laser assisted optoporation. Most laboratories only specify the laser power and exposure time, which worked for the specific group, using their specific equipments and setup. However, contemporary laser optoporation studies are still conducted on systems assembled in-house based on different types of lasers and vary dramatically in their designs. Because the laser optoporation results are related to a lot of parameters such as cell-type, cell-wellness, extracellular environment, and laser system setup, a standard

protocol has to be developed to characterize the laser parameters on a case-by-case basis.

In chapter four of this thesis, I will present a detailed experimental study on standardization of the protocol for the femtosecond laser-assisted optoporation using human embryonic kidney (HEK) cells. A membrane impermeable fluorescent dye and a plasmid DNA carrying the coding sequence for green fluorescent protein (GFP) were employed to analyze the entry of extrinsic molecules into the target cells.

1.4 Integrating the femtosecond laser fabrication with nanoimprinting

Though femtosecond laser induced two-photon polymerization is a versatile nano-fabrication method to investigate cell-environment interaction, it contains a serious flaw; it is a slow point-by-point process. The fabrication process of a nano-structure can last for hours, depending on the complexity and size of the structure. For two-dimensional nano-structures, which have been widely used in studies of cell spreading, adhesion, migration, and differentiation, we have streamlined the fabrication process by combining femtosecond laser fabrication with the nanoimprinting lithography technique[33]. Nanoimprinting lithography has been widely used in making high-resolution structures, such as biomedical sensors and photonic crystals. Traditionally, researchers used expensive cleanroom facilities in conjunction with electron beam lithography (EBL) and reactive ion etching (RIE) to make nanoimprinting molds, resulting in

a complex and lengthy process. Our research has proved that a femtosecond laser is a promising alternative tool to make nanoimprinting molds in an efficient and less expensive way. I will demonstrate in chapter five that the integration of femtosecond laser fabrication with nanoimprinting lithography greatly increased the fabrication speed of making two-dimensional structures. Using the mask aligner and the imprinting mold made by the femtosecond laser, one can quickly transfer the nanopattern of the mold to the biomaterials for fabrication.

1.5 Scope of this dissertation

The objective of this thesis is to investigate the application of a femtosecond laser in the study of a cell-environment interaction *in vitro*. Specifically, I describe the principle, experimental setup, and results of the application of a using a femtosecond laser for both tuning the environment and manipulating cells.

Chapter one provided an overview of the current research of *in vitro* cell-environment interaction and the unique advantages of a femtosecond laser in this research field.

Chapter two describes the fundamentals of laser assisted two-photon polymerization and laser assisted optoporation, as well as the laser mechano-optical system design.

Chapter three introduces negative Poisson's ratio structures, the laser fabrication process of functional negative Poisson's ratio webs, and cell behavior on both negative Poisson's ratio and positive Poisson's ratio webs.

Chapter four standardizes the procedure for laser assisted optoporation of animal cells.

Chapter five evaluates the feasibility to scale up the laser fabrication method by integration of femtosecond laser fabrication with nanoimprinting techniques.

Chapter six provides a summary of previously mentioned work as well as its limitations. The direction of future work is also discussed.

Chapter 1, in part, is a reprint of material that is published as: Zhang W, Chen S. Femtosecond Laser Nanofabrication of Hydrogel Biomaterial. MRS Bulletin 2011; 36 (12): 1028-33

CHAPTER TWO:

The femtosecond laser system

2.1 Introduction of the femtosecond laser

Since its debut in the 1980's, the femtosecond laser has gained ground in a variety of research areas as well as in biological research[82-88]. Two unique features that have made femtosecond lasers particularly desirable are their ultra-short pulse duration, which means very high peak power in the order of megawatts, and their near infrared (NIR) wavelength which is able to penetrate deep into biological sample[89-91]. Because of those advantages, femtosecond lasers have been widely used in three-dimensional nano-scale fabrication through laser induced two photon polymerization, as well as in laser optoporation. I will explain the mechanism of femtosecond laser induced two photon polymerization and the simulation of laser optoporation in cell membrane in this chapter.

2.2 Mechanism of two phonton polymerization

The foundation of two-photon polymerization (TPP) is two-photon absorption (TPA), a process by which one molecule is excited to a higher energy electronic state by simultaneously absorbing two photons. The concept of TPA was first predicted by Maria Goeppert-Mayer in 1931[26]. However, it was not until after the invention of the laser when researchers were able to observe two-photon excited fluorescence in the experiment for the first time. Following the invention of the ultrafast femtosecond laser, researchers have expanded the application of TPA into the micron/nano fabrication field, where TPP was introduced. The peak power of a femtosecond laser is much higher than a

continuous wave (CW) laser or a nanosecond laser. The extremely high photon density in the center portion of femtosecond laser beam allows non-linear laser-material interaction, specifically, two-photon polymerization. Due to the extremely high photon density requirement of TPP and the Gaussian distribution of the laser beam energy intensity over the cross section, the TPP reaction is restricted to the central portion of the laser beam. Thus it is feasible to make features even smaller than the diffraction limit through TPP. This distinction grants a clear advantage to TPP in contrast of traditional single photon polymerization (SPP) [27, 28]. The other advantage of TPP over SPP is the three-dimensional fabrication capability of TPP. A femtosecond laser emits infrared or near infrared wavelength, at which spectra the polymers have negligible absorption. Therefore a femtosecond laser beam is able to penetrate into the photoresist and induce polymerization inside of the liquid without crosslinking the material on its path.

In order to optimize the resolution of TPP and select a suitable TPP material, it is necessary to investigate the mechanism of TPP. Photopolymerization is a chain reaction process that transforms short monomers in liquid state to long polymers in solid state by using light as energy resource. In order to induce this chain reaction, photoinitiator, another ingredient which can easily generate a large amount of free radicals upon laser irradiation, must be added to the monomer solution. The process of TPP is depicted by equation 1 and 2. Equation 1 demonstrates the process of free

radicals generation. In the equation, I is photoinitiator, I* is an intermediate state of the photoinitiator after simultaneously absorbing two photons, $R\bullet$ is free radical. After being generated, free radicals will attack the C=C bonds of the monomers in the solution and produce monomers which contain a free electron, as described in equation 2. The monomer depicted in equation 2 is in a family of materials with acrylic functional groups, which is widely used in TPP. These monomers with a free electron will continue attacking other monomers to form oligomers with free electrons. The chain reaction propagates until two radicals neutralize each other. Since the crosslinked monomer chain forms the backbone of the polymerized solid structure, the chemical and mechanical properties of the solid structure are mostly determined by the monomer. By using different monomers or different molecular weights of the same monomer, polymers with various chemical and mechanical properties can be easily fabricated. Figure 2.1 demonstrates micro-dots array fabricated by the femtosecond laser

$$I \xrightarrow{2\hbar\nu} I^{*} \longrightarrow R\bullet \tag{1}$$

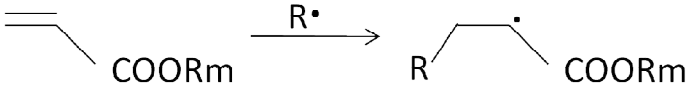

(2)

2.3 Simulation of femtosecond laser ablation of cell membrane

Although the mechanism of optoporation is still not quite clear, various experiments have suggested that femtosecond laser pulses, when tightly focused on a small part of the cell membrane, could cause the formation of a site-specific transient perforation in the cell membrane. The transient perforation can even be smaller than the size of the laser focal volume. To better understand the mechanism of the optoporation process, we simulated the near infrared (NIR) femtosecond laser ablation process with Matlab.

The parameters of the laser we use (Vitesse, Coherent Inc. Santa Clara, CA) are as follows: wavelength λ = 800 nm; repetition rate = 80 MHz; pulse duration = 100 femtoseconds. The numerical aperture (NA) of the oil immersion lens (Fluar, Carl Zeiss MicroImaging, Inc. Thornwood, NY) we use to focus the laser is 1.3. We use water as the aquatic medium in the simulation to simply the calculation. This simplification is proper since the optical properties of the culture media we use (Dulbecco's Modified Eagle's Medium, no phenol red, Invitrogen Inc., Carlsbad, California) is almost identical with water.

$$d = 1.22\frac{\lambda}{NA} \tag{3}$$

Vogel et al. have demonstrate that a high repetition rate femtosecond laser ablates biological material by generating low density plasma within the focus [92]. The low density plasma is formed by multiphoton ionization process. Single photon effect (linear absorption) is neglected for NIR laser interaction

with biological material because biological material is almost transparent (optical window) at NIR region.

To obtain the plasma (free electron) distribution within the focal volume, we need to calculate the laser irradiance distribution first. M. Born et al. revealed that the laser focal region had a shape of ellipsoid [93]. We approximate the length of the short axis of the ellipsoid *d* by the diameter of the Airy disc.

For our case, λ = 800 nm, NA = 1.3, so the short axis *d* is 750 nm. The ratio of the long axis and short axis for the ellipsoid is revealed by Gril et al. [94].

$$\frac{l}{d} = \frac{\sqrt{3 - 2\cos(\alpha) - \cos(2\alpha)}}{1 - \cos(\alpha)} \tag{4}$$

Where α is the opening angle for the objective lens and *l* is the length of long axis. We use the definition of NA to calculate α. For NA = 1.3 and refractive index of water = 1.333, α = 77.2º. So *l*/*d* = 2.4 and *l* = 1800 nm.

Gaussian function is used to simulate the distribution of laser irradiance within the focal region. To simplify the calculation, we use its corresponding time-averaged intensity distribution, which is given by equation 5.

$$I(r,z) = I(0)\exp[-2(\frac{r^2}{a^2} + \frac{z^2}{b^2})] \tag{5}$$

I (0) is the irradiance at the center of the beam at the waist, *a* = *d*/2, and *b* = *l*/2.

We adopt Vogel et al.'s assumption that the free electron density is proportional to I^k, while k is the number of photons required to initiate multiphoton ionization[92]. So the distribution of free electron is derived as equation 6.

$$Q(r,z) \propto \{I(0)\exp[-2(\frac{r^2}{a^2}+\frac{z^2}{b^2})]\}^k \quad (6)$$

Then we use Q (I(0)) to represent the free electron density at the center of the ellipsoid and obtain equation 7.

$$Q(r,z) = Q[I(0)]\exp[-2k(\frac{r^2}{a^2}+\frac{z^2}{b^2})] \quad (7)$$

Since the band-gap energy of water is 6.5 eV and the photon energy of an 800 nm laser is 1.56 eV, 5 photons are required to be sequentially absorbed to ionize water. So *k* = 5 in equation 7.

The normalized distribution of laser irradiance and free electron density are calculated by Matlab® (Mathworks Inc.) and demonstrated in Figure 2.2. The results show that the free electron distribution is much smaller than the laser irradiance. This explains the reason why the femtosecond laser is able to ablate a tiny hole on the cell membrane that is even smaller than the laser focal volume.

2.4 Laser system setup

2.4.1 Optical system design

The most essential part of the fabrication system is the optical system, which consists of a femtosecond laser, optical components, and an inverted microscope, as depicted in figure 2.3. The laser used in the system was a 800 nm Ti:sapphire femtosecond laser. The pulse duration and repetition rate of the laser were 100 femtosecond and 80 MHz, respectively. Since the laser beam coming out of the laser head has a divergent angle of 0.85±0.25 mrad, which cannot be neglected in our application, it must be collimated before being used. A beam expander consisting of two convex lenses was employed to collimate and expand the laser beam. The expanding ratio could be adjusted by using lenses combination with various focal lengths. Meanwhile, a micro-scale pinhole was placed at the focal point of the lenses in the beam expander to filter out the diffraction noise at the periphery of the beam. The size of the pinhole is calculated by equation 8. In the equation, λ is the laser wavelength, f is the focal length of objective lens, and D is the incident laser beam diameter.

$$\text{Pinhole Diameter} = \frac{1.27 * \lambda * f}{D} \tag{8}$$

Various laser powers are needed for different laser application, so a beam polarizer which can continuously adjust laser power is installed in the system. The *in situ* monitoring of the laser experiment is implemented by a

charge-coupled device (CCD) camera. In the meantime, a complimentary high-pass filter is placed in the illuminating system to block out the UV spectra in the illuminating light to avoid overexposure of the sample material during fabrication.

2.4.2 Design of the sample holder and adjust of its levelness

One small but important part in the laser fabrication system which can greatly affect the quality of the result is the sample holder. In order to obtain consistent results over a large area, the sample holder should be able to be adjusted to levelness so the surface of the sample substrate is perfectly perpendicular to the laser beam. A sample holder was made in house to meet such requirements by connecting a mirror mount with a specially designed sample holding board made of aluminum alloy. It was proved in mechanics that the two setscrews on the mirror mount are able to position the sample holding board attached on the mount at any arbitrary angle within its moving range. During the fabrication process, after a drop of prepolymer was placed on the top of the sample substrate, the laser beam with a proper power was employed to make one dot at each corner of the sample substrate. The two setscrews were then adjusted until the dots at the four corners are of the same size, which was the perfect level position.

2.4.3 Automatic controlling system

Another important part of the fabrication system is an automated three-dimensional scanning system which consists of a three-dimensional stage, a laser shutter, and the central controlling program. The pattern to be fabricated was first designed by computer-aided design software AutoCAD, and then the CAD pattern was converted to G-code (a universal controlling code used in computerized numerical control machine) through an open-source G-code converter. For some simple patterns, the G-code can be written by hand. The G-code was customized by the stage manufacturer such that it can be used to both drive an MS-2000 stage in order to control the focal point of our two photon laser system, as well as control the laser shutter-- all in the same script. The G-code was then loaded to Tracer® program which was a control program developed by the stage manufacturer. The Tracer® program controls both the stage and the automated shutter to move the stage and flip the shutter according to the designed pattern. The key to this procedure is the utilization of an incremental or relative coordinate system that moves in relation to the current position. This enabled us to take advantage of the programming language Python and import our code to a python file to make any necessary iterations and scale up to any size we desire. Figure 2.4 shows photos of the fabrication system.

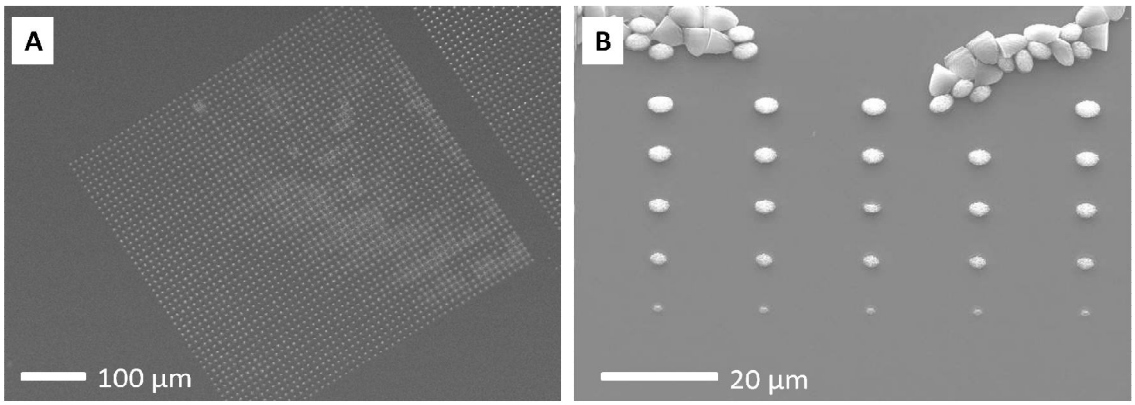

Figure 2.1 SEM images of microdots array made of PEGDA hybrid material

(a) a 500 µm by 500 µm microdots array with dot diameter of 2 µm and a pitch of 20 µm, (b) dose test of microdots fabrication, the focal point of laser beam was lifted from bottom row to top row. As the focal position was lifted, the microdots came off the substrate due to their weak adhesion with the substrate and formed the aggregation above the top row.

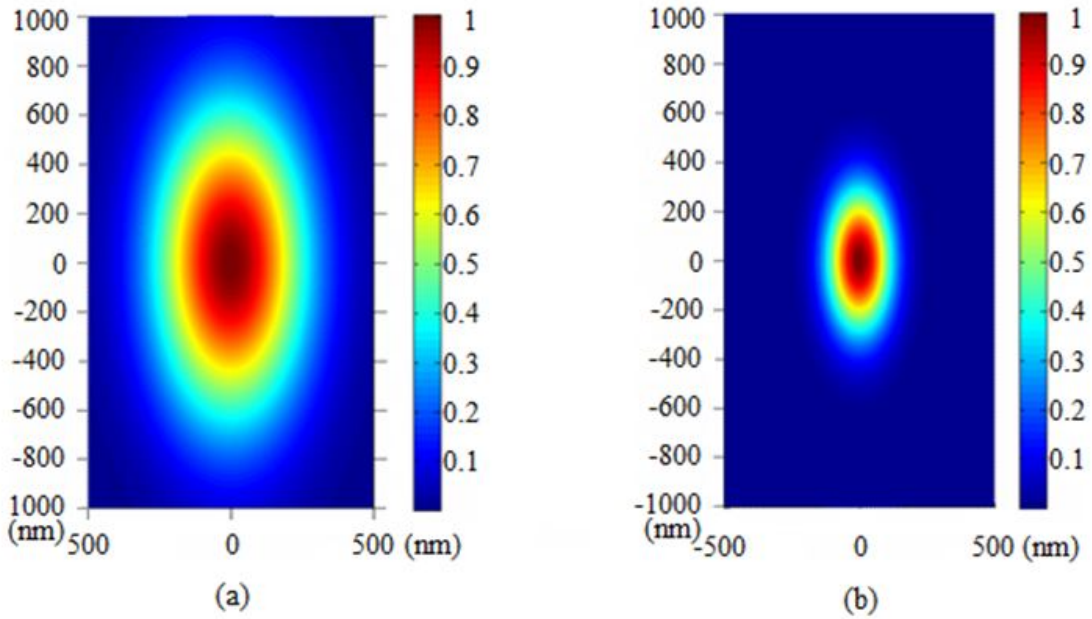

Figure 2.2 Distribution of normalized laser irradiance and free electron

(a) The normalized laser irradiance (unit: W/cm^{2}) distribution in thefocal point. It demonstrates that the irradiance distribution has an ellipsoidal shape, in which the highest irradiance is in the center and the irradiance exponentially decays from inner layer to outer layer. The color bar is the scale of normalized laser irradiance, in which 1 is the normalized irradiance at the center. (b) The normalized free electron (plasma) distribution (unit: cm^{-3}) in the focal point. It shows that the plasma distribution has the same shape as the irradiance distribution but much smaller size, which is the reason why femtosecond laser is able to create a hole smaller than the size of its focal point on cell membrane. The color bar is the scale of normalized free electron density, in which 1 is the normalized density at the center.

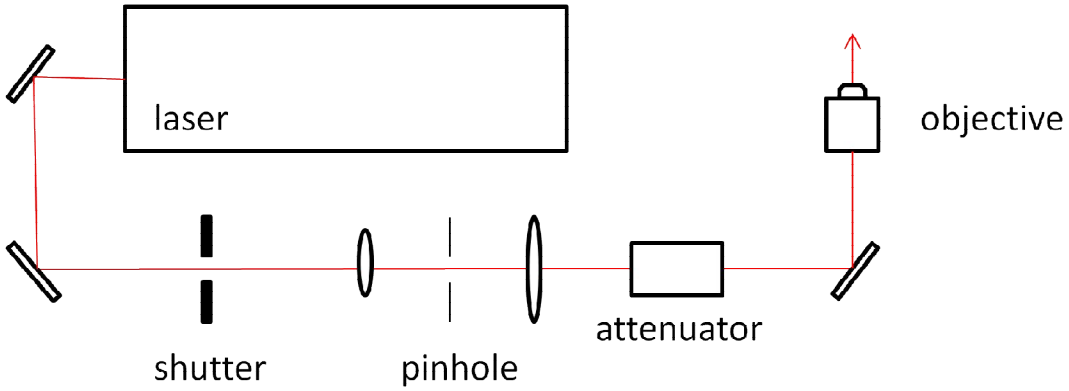

Figure 2.3 Optical design of the femtosecond laser system.

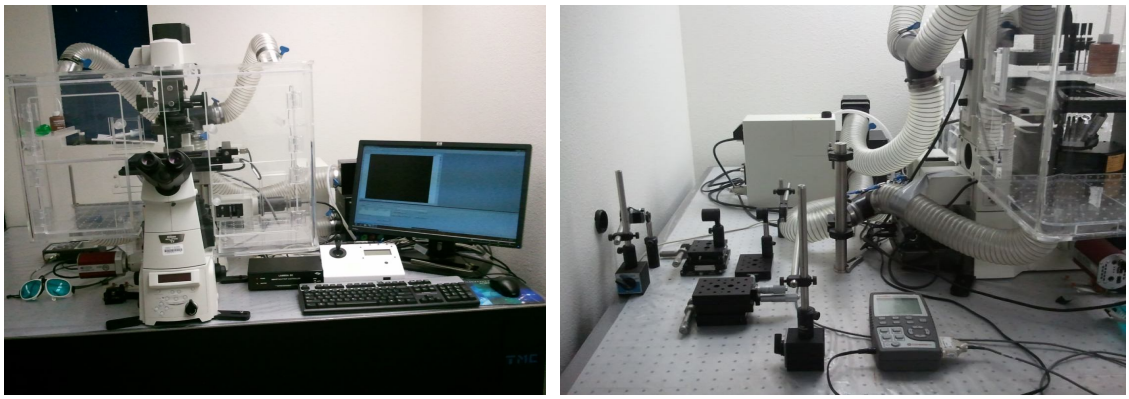

Figure 2.4 Photos of the laser fabrication system

Chapter 2, in part, is a reprint of material that is published as: Zhang W, Chen S. Femtosecond Laser Nanofabrication of Hydrogel Biomaterial. MRS Bulletin 2011; 36 (12): 1028-33

CHAPTER THREE:

Fabrication of negative Poisson's ratio structures and investigation of its influence on cell movement and division

3.1 Introduction

Natural tissues and their cellular microenvironment have complex structural and biological heterogeneity, and are constantly exposed to a myriad of forces. Materials scientists have investigated structure-function relationship of cell-materials interaction, using various approaches. It has been long known that cells generate contractile forces on its underlying substrate [95, 96]. Over the years, researchers have altering the elastic modulus of the interacting substrate by modulating properties such as cross-link density [97], and evaluated cell response. Alterations in elastic modulus of the interacting substrate, both in two-dimensional surface as well as three-dimensional geometry, impact variety of cell types in fundamentally different ways, including motility, gene expression, proliferation, and fate after differentiation[47, 53, 98-102]. These studies have increased our understanding of how cells experience forces, and provided insight into the biophysical mechanisms. However, another fundamental aspect of material properties, the Poisson's ratio has been largely ignored, probably because of the challenges involved in tuning the Poisson's ratio of the biomaterials.

The ability of a biomaterial scaffold to support and transmit cell and tissue forces can be quantitatively described by its elastic modulus and Poisson's ratio. Elastic modulus quantifies a scaffold's elastic behavior in the loading direction, while Poisson's ratio describes the degree to which the scaffold contracts/expands in the transverse direction, perpendicular to the

loading direction (figure 3.1). Typically Poisson's ratio is assumed to be positive for all materials (~0.3 to 0.5), even though materials with negative as well as zero values do exist in nature. A positive Poisson's Ratio materials contract transversally when stretched, while a Negative Poisson's Ratio (NPR) materials expands in both the axial and transverse directions. In nature, we come across several materials with a NPR or *"auxetics",* such as in crystalline materials[103-108], carbon allotropes [109], foams [110-112], polymers and laminates [113-116], and other extreme states of matter [117-120]. Although, for naturally occurring materials, the NPR property seems to be an intrinsic property of the material and cannot be tuned according to specific applications. Tuning the Poisson's ratio requires control over pore-interconnectivity and internal architecture of a material, which can be quite difficult to achieve. Artificial auxetics have been developed by incorporating rib-containing pores, which modify the shape and deformation mechanisms of polymers, transforming their mechanical behavior to exhibit NPR property[110, 112, 114, 121-125]. These polymers demonstrate well-defined strain-dependent NPR behavior [110, 119, 126, 127], however, the response is "process dependent" and cannot be tuned according to a specific value of Poisson's ratio. For example, polyurethane foams annealed in a compressed state naturally re-organization their cellular microstructure and exhibit NPR behavior [110, 121] However, processes such as annealing have little control over the reorganization of cellular microstructure comprising the foams, making it difficult to tune the Poisson's ratio according to a specific application. There is

also evidence of negative and zero Poisson's ratio materials in biology [103, 128-134]. To investigate cell-materials interactions, Poisson's ratio has to be precisely tuned, both in magnitude and polarity. Some tissue engineering applications need unique strain response, wherein biomaterials having a negative or zero Poisson's ratio may be more suitable for emulating the behavior of native tissues. Recently, we developed micron-scale scaffolds which exhibit negative, positive and zero Poisson's ratio in PEGDA biomaterials [135-137]. Although these scaffolds themselves exhibited NPR behavior, a single cell is not able to sense the effects of the altered Poisson's ratio at micron resolution (~50-100μm). In this study, we use femtosecond laser to fabricate suspended web structure with tunable Poisson's ratio, and utilize these sub-micron structures to evaluate cell response.

3.2 Materials and Methods

3.2.1 Preparation of polyethylene glycol diacrylate (PEGDA)

PEGDA (MW 700) was used to make the webs because of its biocompatibility. PEGDA pre-polymer was prepared as follows. First, PEGDA was mixed with Milli-Q water at a ratio of 1:4, 4% (w/v) and lithium phenyl-2,4,6-trimethylbenzoylphosphinate(LAP), prepared as the protocol described by Fairbanks et al (need reference) was added to PEGDA as the initiator. 5mM acrylate-PEG RGDS peptide was then added to PEGDA to promote cell

adhesion. The solution was mixed by a vortex mixer for 5 minutes and was then purified through a 0.22 μm pore size syringe filter.

3.2.2 Preparation of sample substrate

A piece of glass coverslip was used as the sample substrate for the webs. The coverslip was coated with a thin layer of PEGDA to prevent cell attachment on the substrate. Before being coated with PEGDA, the coverslip was methacrylated to enhance the adhesion of the PEGDA thin layer on the surface of substrate.

(a) Methacrylation of glass coverslips

First, the glass coverslips were cleaned for 5 minutes in piranha solution consisting of 35mL sulfuric acid and 15mL hydrogen peroxide. Then the coverslips were taken out of the piranha solution and washed for 5 times with Milli-Q water. After that, the coverslips were immersed in ethanol for 5 minutes to remove residual water. In the meantime, methacrylation solution was prepared by mixing together 1mL 3-(trimethoxysilyl)-propyl methacrylate, 50mL ethanol, and 6mL of 1:10 galcial acetic acid (acetic acid in ethanol). The coverslips were dried by compressed air and immersed in the methacrylation solution overnight. On the next day, the coverslips were taken out of the methacrylation and were cleaned with ethanol and dried with compressed air, sequentially.

(b) PEGDA coating of glass coverslips

After the methacrylation process, the coverslips were coated with a thin layer of PEGDA to prevent cell attachment on the surface. We used 20% PEGDA (80% water) as the coating material because it has much lower swelling ratio than the 100% PEGDA does. To facilitate polymerization, 2% (w/v) LAP was added to the solution as the photoinitiator. The thin layer of PEGDA was generated by sandwiching the 20% PEGDA between one piece of methacrylated coverslip and one piece of untreated coverslip. The untreated coverslip was cleaned with ethanol before use. A pipettor was used to transfer 7 µl PEGDA onto the surface of metharylated coverslip and the untreated coverslip was covered on top of the metharylated coverslip. The sandwich structure was placed on an experiment table for 3 minutes to stabilize. After that, it was irradiated by a UV lamp for 1 minute to polymerize the PEGDA layer. Then the two pieces of coverslips were detached from each other by hand.

In order to culture cells on the coverslip, the coverslip must be attached to a petri dish, which can hold cell culture medium. A 10mm x 10mm hole was cut on the bottom of a 35mm plastic petri dish with a single edge cutter blade and the PEGDA coated coverslip was glued onto the bottom from outside. The glue we used was dipentaerythritol pentaacrylate with 1% photoinitiator (Irgacure 819). A UV lamp was used to cure the glue. After the PEGDA-coated coverslip was glued on the bottom of the petri dish, 4 mL water was filled into

the petri dish to maintain the water content of the PEGDA coating on the coverslip.

3.2.3 Femtosecond laser fabrication of the webs

Figure 3.3 shows the schematic drawing of the femtosecond laser fabrication system setup. The laser source was a Ti:sapphire femtosecond laser producing 100-femtosecond wide pulses at a repetition rate of 80 MHz with a maximum power of 350 mW. The central wavelength of the laser is 800 nm and the diameter of the beam out of the laser head is 1 mm. The laser beam was expanded by a 4X beam expander to make full use of the aperture of the objective lens. Then the laser beam was guided by a group of mirrors into an inverted microscope and focused by an oil-immersion objective lens onto the sample which was mounted on a motorized stage. The laser power can be continuously adjusted by an attenuator. The scanning of the sample was implemented by simultaneously controlling the stage and an electrical-motorized shutter using the microscope software. The laser power employed for the fabrication was 50 mW, measured by a power meter before the laser beam entered the objective lens. The scanning process was monitored *in situ* by a charge-coupled device (CCD) camera.

Before making the structures, a drop of immersion oil was placed on the objective lens. A pipettor was used to drop 20 µl of the 20% PEGDA prepared in step 1 on the bottom of the petri dish. The petri dish was then secured on the

stage by two strips of double-side tape. After that, the objective lens was lifted to get in touch with the bottom of the petri dish. As the objective lens was going up, a series of dots were made by the laser beam to locate the position of the coverslip surface, where the structure would be attached to.

An array of 7 supporting walls was fabricated first to hold the auxetic and non-auxetic webs. The supporting wall was an 8-layer wood-pile structure with the size of 120 μm (length) x 6 μm (width) x 12 μm (height). Each supporting wall was fabricated by the laser in a layer-by-layer mode with a fabricating speed of 0.05 mm/second and a laser power of 70 mW. After the supporting walls were made, the laser beam was focused on top of them to make the webs. The two edges of each web were attached to two adjacent supporting walls. Since the PEGDA pre-polymer had enough density and viscosity to support polymerized structure, the webs did not drop or move around while being made. The fabricating speed of the laser was 0.65 mm/second and the laser power being used was 45 mW. The auextic and non-auxetic structures were fabricated on the supporting walls alternatively.

After the webs were fabricated, the unpolymerized PEGDA was washed away by Milli-Q water. Then the petri dish was filled with phosphate buffered saline (PBS) which contained 2% penicillin-streptomycin (PS) to sterilize it. After that the petri dish was kept in a 37 ºC incubator for future cell seeding.

3.2.4 Femtosecond laser fabrication of fluorescence-labeled webs

Fluorescence-labeled webs were fabricated with the same system setup and parameters. The only difference was that PEG-RGD-FAM was added to PEGDA at 0.5mg/mL to incorporate fluorescent peptide into the webs. After laser fabrication, the webs were rinsed 5 times with Milli-Q water for 5 minutes each to get rid of the unattached PEG-RGD-FAM.

3.2.5 Cells maintenance and seeding

10T1/2 cells (American Type Culture Collection, Manassas, VA?) were maintained in Dulbecco's modified eagle's medium with high glucose (DMEM) (Gibco, North Andover, MA) supplemented with 10% fetal bovine serum (FBS). The cells were cultured in an incubator with 5% CO2 concentration and 37 ºC. The culture medium was replenished every other day and the cells were splitted as necessary.

Prior to cell seeding, the petri dish with the webs was washed twice with PBS. Then it was filled with 3 mL pre-warmed DMEM supplemented with 10% FBS and 1% PS. Throughout this process, caution must be taken to keep the webs in liquid to prevent them from collapsing. An ethanol-washable marker was used to mark the position of the webs on the bottom of the petri dish to facilitate cell seeding. A seeding density of 5,000 cells per petri-dish was used and the proper cell density was achieved by centrifugation and resuspension of cells. A drop of 10 µl medium with proper cell density was carefully added on

top of the webs. While adding, the pipette tip was made in touch with the surface of the medium to make sure the cells were seeded on the webs. After that, the petri dish was left in the biosafety cabinet for 5 minutes to help the cells to stabilize.

3.2.6 Time-lapse imaging

Time-lapse images were taken in a microscope (Nikon) with a cell culture chamber (*In vivo* Science?) after the cells were seeded on the webs. The CO2 concentration and the temperature in the cell culture chamber can be maintained at 5% and 37 ºC, respectively. The bottom of the chamber was filled with DI water to maintain the humidity. The heater of the chamber was turned on 4 hours before the time-lapse imaging to achieve a stable 37 ºC environment. The petri dish with cells attached to the webs was then fixed on the microscope stage by two strips of double side tape. After that, the doors of the chamber were closed and the CO2 valve was opened. A 40x objective lens was used to take the time-lapse images. Images were taken every two minutes at a range of z positions with a step of 2 μm. With the same setup, fluorescent time-lapse images were taken to monitor the nucleus activity of the cells. Hoechst 33342 was added to the medium at 1 μg/mL for live cell imaging.

3.2.7 Immunofluorescence labeling

EdU staining was conducted with the Click-iT® EdU imaging kit (Invitrogen, Carlsbad, CA) following the protocol provided by the manufacturer.

After the cells were seeded on the web for 12 hours, EdU was added into the medium at 10 μM and the cells were cultured in the incubator for another 12 hours. After the incubation, the medium was removed and the sample was fixed with 0.5 mL of 4% formaldehyde in PBS for 15 minutes at room temperature. Then the formaldehyde was removed and the petri dish was rinsed twice with 1 mL of 2% BSA in PBS for 5 minutes each. After being permeablized with 1mL of 0.5% Triton X-100 in PBS for 20 minutes, the sample was again rinsed twice with 1 mL of 2% BSA in PBS for 5 minutes each. Then the sample was incubated in the Click-iT® reaction cocktail which contained Click-iT® reaction buffer, $CuSO_4$, Alexa Fluor® azide, and reaction buffer additive for 30 minutes at room temperature, protected from light. After the reaction cocktail was removed, the sample was rinsed once again with 1 mL of 2% BSA in PBS for 5 minutes.

PBS was then used to wash the sample for DNA staining. The sample was incubated with 2 mL of 5 μg/mL Hoechst 33342 in PBS for 30 minutes at room temperature, protected from light. Then the Hoechst solution was removed and the sample was washed twice with 3 mL of PBS.

For focal adhesion staining, the sample was first blocked for 60 minutes in blocking buffer containing 2% bovine serum albumin (BSA), 0.3% Triton X-100, and 97.7% PBS. Then primary antibody solution, which was 0.5% monoclonal anti-vinculin in blocking buffer, was applied onto the sample and the sample was incubated overnight at 4 ºC. After being rinsed three times in PBS

for 5 minutes each, the sample was incubated in the secondary antibody solution consisting 1% Alexa Fluor 647 goat anti-mouse IgG in blocking buffer for 60 minutes at room temperature. The sample was once again rinsed three times in PBS for 5 minutes each. All steps were protected from light. After the immunofluorescence staining process, the sample was kept in 4 ºC and protected from light.

3.3 Experiment design and results

3.3.1 NPR web design and fabricaiton

Figure 3.2A highlights the geometry and dimensions of unit-cell type; the reentrant and cut missing rib designs for NPR behavior. Structural support beams were incorporated at the ends of each web structure, to ensure that the structure is suspended, and cell will be able to apply strains and freely move the structures (figure 3.2B). Similar structure made on a flat surface, can be actuated by addition/removal of water, and could be moved by the cells, however, in order to study effects of cell movement only on the web, we have to suspend the structure between two supporting beams.The reentrant structure (figure 3.2A) is formed by changing the four side angles (angle ζ) between the vertices (ribs) in a six-sided honeycomb (hexagon), with some additional modifications [126, 138]. Two rib lengths, L_1 and L_2, constrain the dimensions of the unit-cell, including angle ζ (the value of angle ζ is set by the rib-length ratio and is not arbitrarily set), and the ratio of the two rib lengths has a sizable influence

on Poisson's ratio. The dimensions used are shown in figure. Varying angle ζ alters the magnitude of Poisson's ratio, which gives Poisson's ratio its strain-dependent response. Two-photon polymerization within the concentrated focal region was used to fabricate both the supporting structures as well as the suspended web structures. A Ti:sapphire femtosecond laser is tightly focused onto the appropriate z plane in the volume of the photosensitive PEGDA prepolymer, and 3D structures were fabricated by moving the stage in XYZ (figure 3.3). PEG biomaterial was chosen, because of it high water content and biocompatibility and tunable mechanical properties [97, 139]. Photosensitive prepolymer solution was prepared by adding biocompatible initiator, lithium phenyl-2,4,6-trimethylbenzoylphosphinate (LAP) and acrylate-PEG RGDS peptide to 20% PEGDA (80% DI water) solution. Methacrylated glass surface was coated with 20% PEGDA solution without the peptide, to prevent cell adhesion onto the glass surface.

Visualization of the web-structures using scanning electron microscopy (SEM) resulted in collapsed web structures, even with critical point drying technique. As a result, the suspended structures were visualized by introducing PEG-RGD-FAM in the prepolymer solution (figure 3.2B).

3.3.2 Cell experiment

To evaluate cell response, 10T1/2 cells were seeded on the web structures and cell movement was monitored using time-lapse microscopy

technique. 10T1/2 are anchorage dependent cells, an embryonic fibroblast cell line that differentiates into perivascular cells *in vivo*, typically used to stabilize a functional microvascular network. As cells move on NPR web structures, they apply forces to the underlying substrate with focal adhesions, and deform the web in various configurations (figure 3.4A). The webpoints deformed by the cells return to the original position, when cells disengage and stop applying forces. The NPR web responds and accommodates strains due to different cellular forces as shown in the schematic (figure 3.4C). On the NPR web, the web points have the ability to move significantly (Δy = -6 to +12microns; Δx = -3 to +4) as compared to PPR web points (Δy=-1 to +2) and (Δx=-3 to +2) (figure 3.4B). When a NPR unit cell expands in the x and y axis; for every 0.9μm X displacement, there is a corresponding increase in Y by ~8μm (figure 2A). Web movement seen in PPR web, is the noise in the system, caused by the suspended nature of web in liquid medium. In the unit-cell models of re-entrant or NPR structure (figure 2A), the position and arrangement of the ribs relative to one another engender a negative Poisson's ratio by virtue of a combination of rib bending (flexure), stretching, and hinging (angular deformations) [123, 126, 138, 140]. The degree to which each structure deforms depends on unit-cell geometry, the bulk material properties of the ribs and the direction of loading. According to the simple hinging model reported by Gibson and Ashby [140], axial strain causes solely a change in angle ζ while the magnitude of the negative Poisson's ratio depends upon both ζ and the ratio L_2/L_1, where the rib length

ratio is assumed to stay. For $L_2/L_1 = 1.33$, which gave an undeformed angle ζ of approximately 40°, the hinging model yields a theoretical Poisson's ratio of approximately -1 at zero strain that linearly decreases to about -0.7 for axial strains of 0-0.2. However, since multiple cells apply forces in many different directions on the NPR web, the Poisson ratio change depending on proximity to cell/s and force transmission from other cells on the web (figure 3.4C). Some web points experience cellular pulling forces from adjoining cells on the web, while others experience inward pulling forces by the cell, while webpoints with no cellular forces remain neutral. Since Poisson ratio is calculated by measuring the transverse displacement of web points when axial forces are applied, for this particular case, it is difficult to measure the Poisson's ratio of the overall structure, since each NPR unit cell feels stresses from all the cells on the web, applied in a variety of XY directions. Therefore, idealized Poisson's ratio of unit auxetic structures were calculated by assuming the force application on either X or Y axes, and are the results are denoted by υ_{XY} and υ_{YX} (figure 3.4D). Since the overall displacement in Y axis is larger, we get higher NPR for NPR-XY, but both XY and YX Poisson ratios are negative as expected. On auxetic webs, any cellular force is easily transmitted to other webpoints away from the source, because of the of local biaxial expansion/compression behavior. Fluorescent time-lapse images were also taken to monitor the nucleus activity of the cells using Hoechst 33342. The images clearly demonstrate the movement of cells on NPR and PPR webs.

3.3.3 Immunofluorescence staining results

Immunofluorescence staining was carried out to evaluate placement of cell adhesion sites by labeling for actin and focal adhesion sites using monoclonal anti-vinculin, as well as cell proliferation using EdU staining, on NPR and PPR web structures (figure 3.5). On NPR web, the cells seem to spread almost immediately after seeding, evident from actin staining (white arrow) (figure 3.5A-C). Cells tend to be randomly oriented. The pseudopods of the spread cells do not align along the suspended NPR struts, a feature typically seen with surface topographies on surface. Cell on PPR web are not able to spread in the first two hours, and most of the cells adhere to the support structures, however, some spreading is seen at later time points (>3hours). Cells adhere to the suspended (figure 3.5D, E) web structures through integrin-mediated adhesions. Figure 3.5G-H shows vinculin labeling throughout the cells, which indicated small (< 0.25μm) nascent adhesions while strong labeling on some of the locations indicate larger (>1μm) focal adhesions. The optimization of fabrication conditions can be used to manipulate number of FA formation, by controlling the number of adhesion site growth, since the cells can only bind to the web structures, and any change in the resolution of the width will result in change in the formation of FAs. This can be potentially used as a way to have direct control over adhesion sites. Variety of micron and nano-scale topographies can be fabricated using this technique, to evaluate cell response such as cytoskeleton formation, spreading, and proliferation.

3.3.4 Abnormal cell divisions

Abnormal cell divisions were observed on the NPR web region (figure 3.6). Cell division, a critical aspect of all multicellular organisms, requires segregation of chromosome facilitated by physical division of the cytoplasm, resulting in separate daughter cells. In normal cell division, during telophase, the cleavage furrow ingresses resulting in compression of the central spindle to form an intercellular microtubule bridge called the midbody. The midbody is severed, resulting in the final separation of daughter cells. On NPR webs, cleavage furrow ingression began normally; however, the resulting daughter cells remain attached to each other for the duration of the experiment (~12 hrs). In one case, (figure 3.6A-F) one cell resulted in formation of a long structure, and probably underwent apoptosis after being unable to complete abscission. In another case (figure 3.6G-L), midbody regressed after failing to separate, giving rise to a multinucleated cell, then reentered mitosis however the midbody persisted, and did not break off after the onset of cytokinesis. In another case where fluorescent time-lapse images were taken (figure 3.6M-R), two nascent daughter cells moved on the web hand by hand, all the while maintaining the midbody connection. Since cell division failure can cause genetic instability, ultimately leading to cancer[141] researchers have elucidated molecular mechanism of abnormal cell division using several midbody components. Cytokinesis failure and associated behavior has been reported following depletion of components of the cortical cytoskeleton, such as anillin, septins,

formins[142-144]. Our observations suggest that similar unusual cell division can be induced solely by the NPR structure, in absence of any manipulations to the cell components. Arrows indicate symmetric as well as asymmetric furrow formation during cell division on NPR webs. During cell movement, bleb formation and constantly extending and retracting protrutions are also seen on NPR webs. NPR property affect the spatial distribution of adhesive contacts a cell experiences during cell division and movement. The unusual cell response most probably affects recruitment of specific proteins involved in cell adhesion, actin polymerization and microtubule stabilization.

3.4 Conclusions

Normal tissue cells probe elasticity as they anchor and pull on their surroundings, and respond through cytoskeletal reorganization and associated processes. Cells adhere to solid substrates that range in stiffness from soft to rigid and that also vary in topography and thickness. NPR web and similar web of various geometry, shapes, as well as resolution, in terms of both the thickness as well as width, can be used for evaluating cells response on a web. Most tissue cells not only adhere to but also pull on their microenvironment and thereby respond to the mechanical properties of substrates in ways that relate to elasticity, however so far only one component of elasticity, i.e. elastic modulus has been investigated. This work potentially opens doors to evaluating Poisson's ratio by keeping the bulk elastic modulus constant. Researchers have investigated cell behavior on substrates with gradient elastic modulus[100],

however, using this technology, a gradient Poisson's ratio web can be fabricated, which is able transmit cellular forces across a range of Poisson's ratio on a single substrate. We hope that this technique will be used by researchers to investigate effects of altering the Poisson's ratio on variety of cellular aspects including morphology, gene expression, migration using different cell types. The methodology developed in this work will foster experiment and contribute to the broad field of mechano-biology.

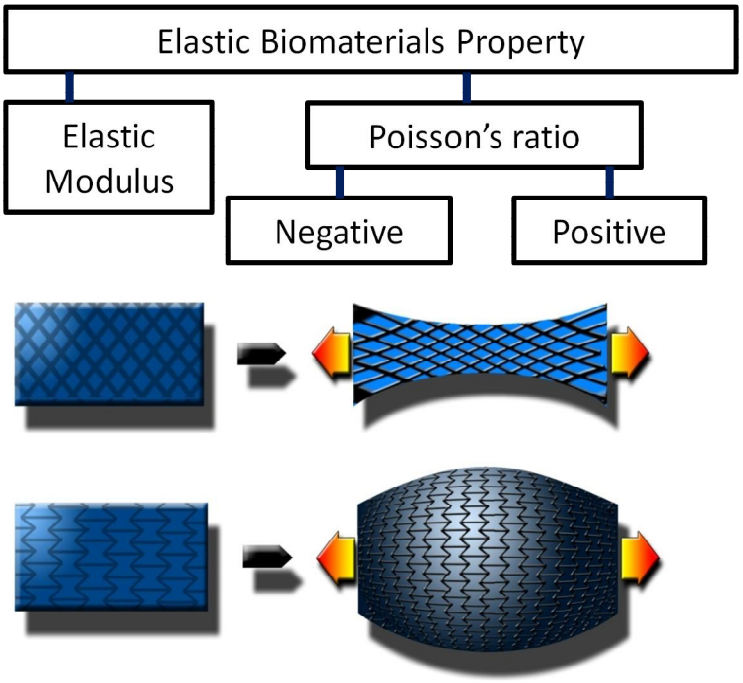

Figure 3.1 Schematic drawing of negative Poisson's ratio and positive Poisson's ratio

The elastic property can be comprehensively expressed by the elastic modulus and the Poisson's ratio. Schematic shows a positive Poisson's Ratio (PPR) materials contracting transversally when axially stretched, while a Negative Poisson's Ratio (NPR) material expanding in both the axial and transverse directions.

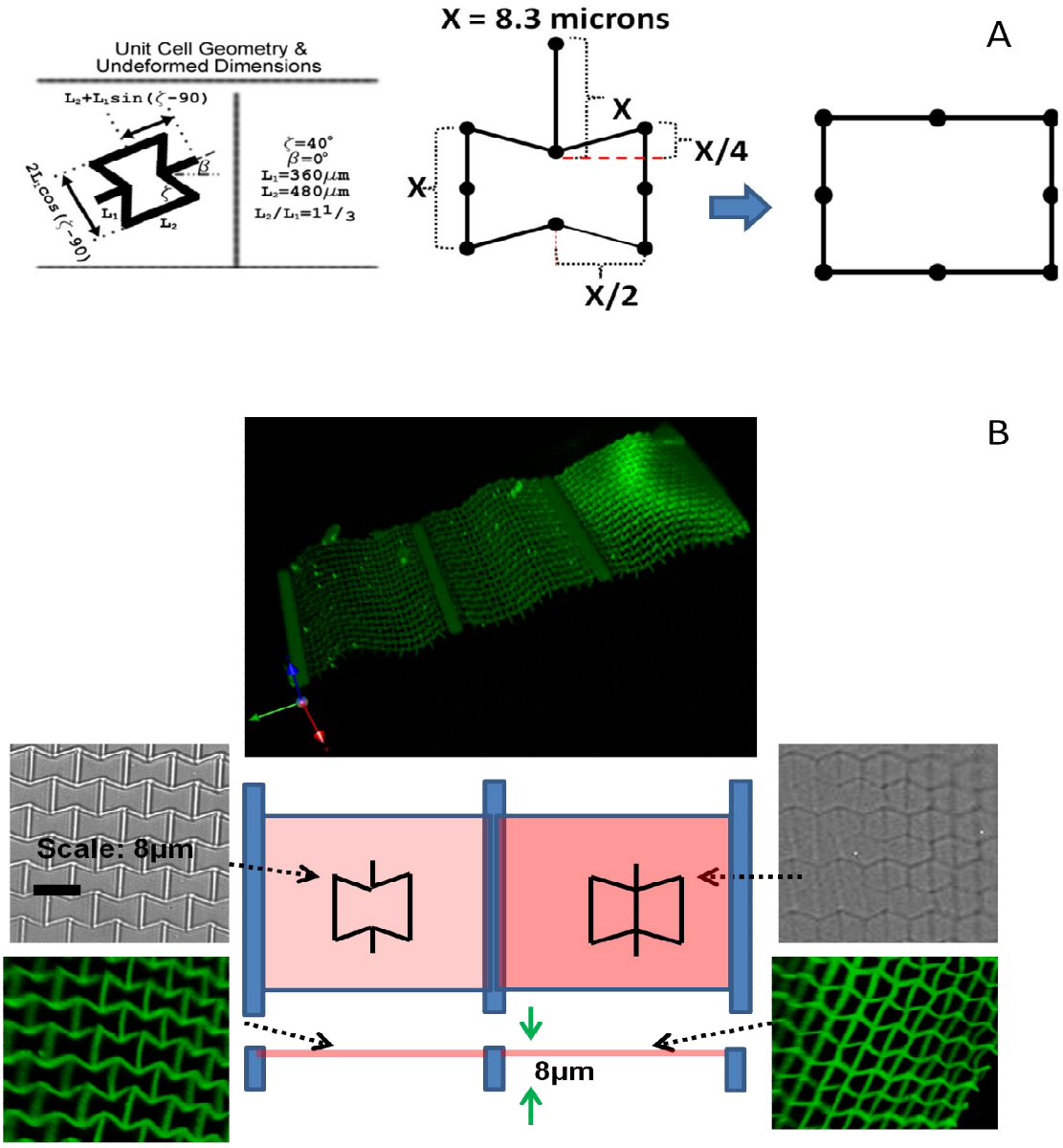

Figure 3.2 Bright field and fluorescent images of NPR and PPR webs

(A) Re-entrant honeycomb configuration was adopted as the uni-cell geometry for the NPR web, while an additional strut modification to the NPR structure served as the positive control. Schematic shows that with axial strains, (Green arrows), the unit-cell exhibits a NPR response (Red arrows), by virtue of the position and arrangement of the struts relative to one. (B) NPR and PPR over-hanging web structures were fabricated with side supports. Figure shows the optical and confocal image of the suspended structures in PEGDA biomaterial.

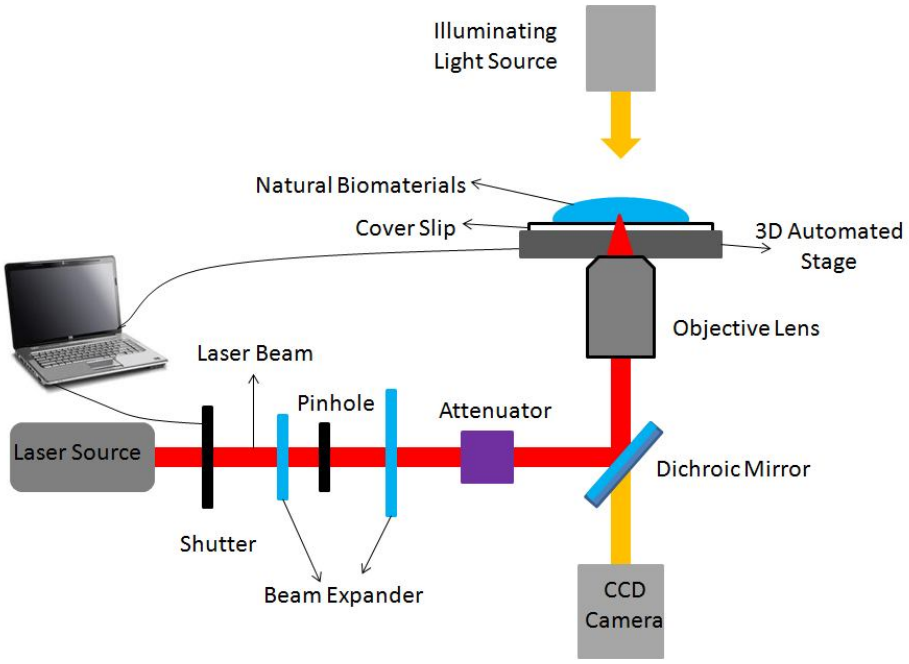

Figure 3.3 Schematic design of the femtosecond laser fabrication setup

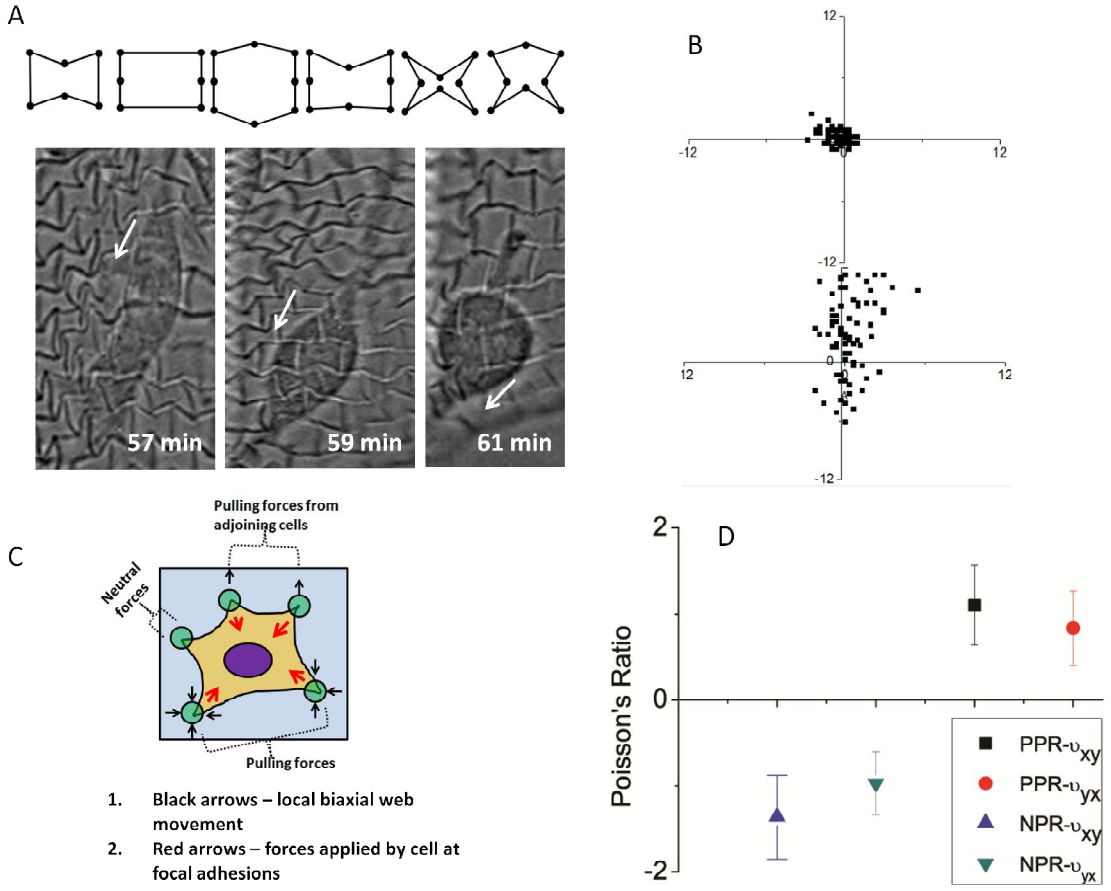

Figure 3.4 NPR and PPR webs moved by cells

(A) The suspended structure exhibit NPR behavior as a 10T1/2 cell moves across the web structure. White arrow indicates the direction of movement with associated time-stamps. (B) Frame-to-frame trajectory of multiple webpoints (in microns) after 10T1/2 cell seeding on web structures. This analysis represents data pooled from different locations on the web structures for 2 hours with 8 min interval. (C) Schematic showing the different forces on the webpoints. (D) Graph shows idealized Poisson's ratio with application of strains in X and Y direction. Since the overall displacement in Y axis is larger, we get higher NPR for NPR-XY, but both XY and YX Poisson ratios are negative as expected.

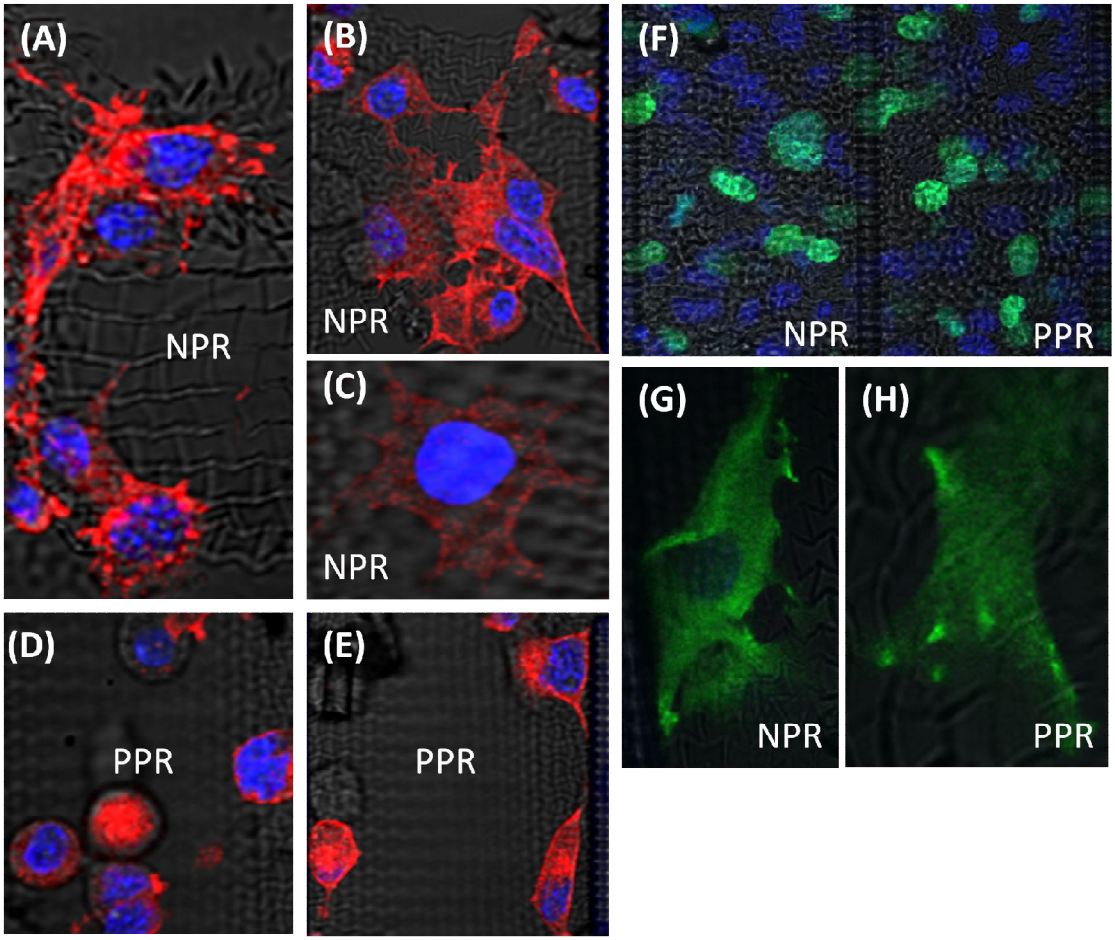

Figure 3.5 Immunofluorescence staining of 10T1/2 cells on NPR and PPR webs

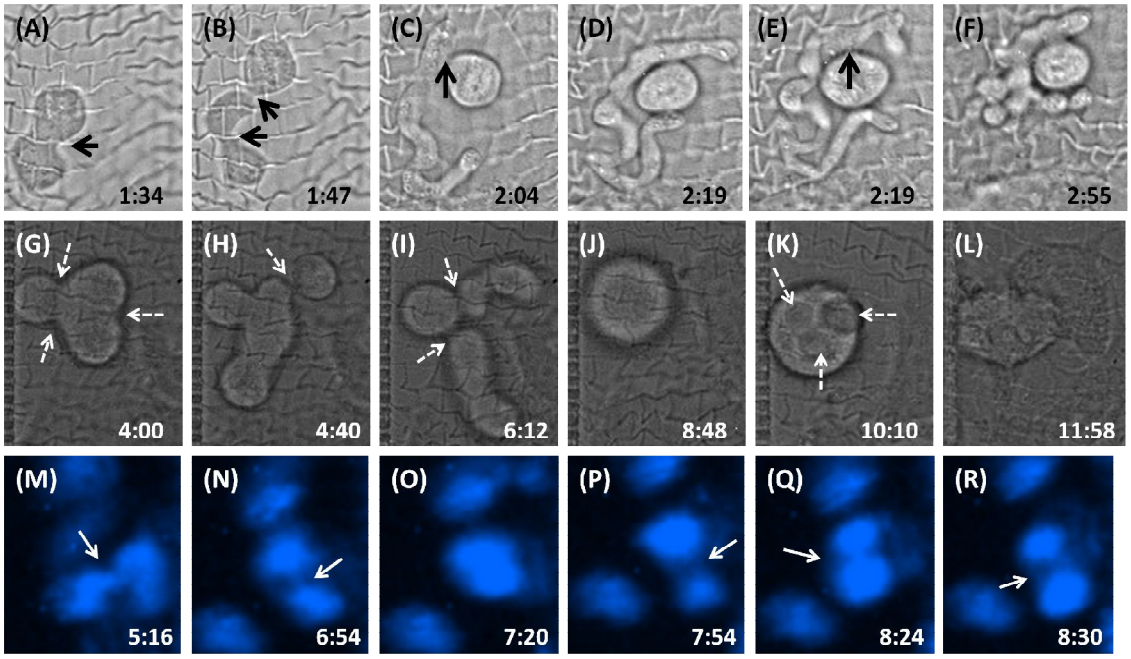

Figure 3.6 Abnormal cell divisions on NPR webs in both bright field and fluorescent views

(A)-(F) Two daughter cells had difficulty separating from each other and one daughter cell became snake-like cell; (G)-(L) Three nucleus appeared in the cell after the daughter cells could not separate from each other; (M)-(R) Live nucleus staining time-lapse images of two daughter cells could not detach from each other.

Chapter 3, in part, is in preparation for submission as: Zhang W, Soman P, Meggs K, Qu X, Chen S. Influence of Negative Poisson's Ratio on Cell Movement and Division

CHAPTER FOUR:

Femtosecond laser-assisted optoporation for drug and gene delivery into single mammalian cells

4.1 Introduction

Traffic of molecules in and out of living cells is tightly regulated by the plasma membrane. This barrier of phospholipid bilayer is generally selective against hydrophilic and charged molecules as well as various macromolecules including nucleic acids, peptides and proteins [145]. Targeted and reversible permeabilization of the plasma membrane is of paramount interest in today's biology and biotechnology. For example, to analyze the behavior of drugs and substrates or inhibitors for certain enzymes or to localize cellular proteins by fluorescence-based immunocytochemistry, the delivery of the given reagents or antibodies into the cell interior is an absolute prerequisite. Ideally, these observations should be made in the intact "live" cells to harness the most reliable and biologically relevant data [146-148]. However, such real-time observations can be challenging as seen in cellular imaging, in which most of the commonly used techniques requires fixation and detergent-based membrane permeabilizaion to deliver the antibodies or dyes into the cell interior [149].

Transfection of cultured mammalian cells is also one of the indispensable techniques in biomedical research laboratories. Hydrophilic DNA molecules are commonly introduced into cells using either liposomal or cationic chemical delivery vehicles, viral vectors, or physical permeabilization such as electroporation [69, 150]. Liposomal delivery and electroporation are sometimes also used for the injection of compounds other than nucleic acids [64, 151, 152].

These methods allow manipulations and analyses of intact cells. However, in most cases, cells are treated as a population and the produced data only represents the average of the whole group. Single-cell manipulation and analyses has been drawing attention recently since It is well accepted that there are cell-to-cell variabilities in many biological aspects, and analyses of individual cells could often provide a wealth of information [153]. As the notion of lab-on-a-chip (LOC) [153] and lab-in-a-cell (LIC) [154] emerged as devices for high throughput single cell analyses, there is an immediate need for a quick, efficient and versatile method to deliver extrinsic compounds and reagents into single cells.

Optical-poration or optoporation has recently been receiving much attention as a promising method for easy and efficient delivery of extrinsic compounds into single live cells. Femtosecond laser can produce a tiny, submicrometer-sized pore, which lasts for a fraction of a second, at a defined location on the plasma membrane of a target cell to facilitate introduction of membrane impermeable substances such as foreign DNA. Femtosecond laser has been used by several groups for a number of cell lines, reporting cell viabilities from 50% to 100% using a variety of impermeable substances [70-77]. Laser optoporation is compatible with standard microscopy optics, coverslip configuration, microfluidic applications. Single cell manipulation using the femtosecond optoporation technique could have far reaching consequences in the field of bioengineering, tissue engineering and stem cell therapy [72].

There is, however, a major hurdle towards establishing the point-and-shoot cellular optoporation with femtosecond laser: the process must be standardized for each specific cell line. Several parameters such as (a) exposure time (b) laser power and (c) location of irradiation need to be characterized for best and reproducible results. Optimization of these variables can be daunting and time-consuming since the focused laser has to be manually aligned onto the plasma membrane of several, if not dozens of, cells. Also in many experiments using live cell culture, the specific cells treated with the laser have to be re-located after several hours or days of incubation to investigate the effects of genes, indicators, antibodies and other compounds introduced into the target cells [70, 72]. Lack of standardization seems to be the reason for discrepancies in previously reported values for laser parameters. Most laboratories only specify the laser power and exposure time, which worked for the group, using their specific equipments and set-up. Most contemporary laser ablation studies are still conducted on systems assembled in-house based on different types of lasers and vary dramatically in their designs. Often, this results in disagreements between groups regarding the type of instrumentation needed for a particular task. In this work, we present a detailed experimental study on standardization of the protocol for the femtosecond laser-assisted optoporation using human embryonic kidney (HEK) cells.

4.2 Materials and methods

4.2.1 Cell culture and preparation

All optoporation experiments were performed using 35 mm petri dishes with poly-D-lysine coated glass bottom of 10 mm diameter and 0.17 mm thickness (Model Number: P35GC-0-10-C, MatTek Corporation, Ashland, MA). A 4 X 4 square grid with each square area of about 200 μm X 200 μm was manually scratched on the bottom side (outside) of each dish using a tungsten carbide scriber. Human embryonic kidney (HEK) 293H cells were maintained in Dulbecco's Modified Eagle Media (DMEM, Invitrogen, Carlsbad, CA) with 10% v/v Fetal Bovine Serum (FBS, Atlanta Biologicals, Norcross, GA) and 1X Antibiotic/Antimycotic Solution (Cellntec, Switzerland) in a humidified incubator at 37°C with 5% CO_2. Cells were seeded on the glass bottom dish with 1 mL culture medium without phenol red and grown for 48 hours to achieve 10-30 % confluency before laser treatment.

4.2.2 Laser instrumentation set-up

Figure 1 shows the experimental setup of the femtosecond laser assisted optoporation. Ti:sapphire femtosecond laser (Vitesse, Coherent Inc. Santa Clara, CA) used for optoporation experiments produce 100-femtosecond duration pulses at with a central wavelength of 800 nm at 80 MHz frenquency. The femtosecond laser beam was expanded by a homemade 2X beam expander before it was focused on the cell membrane by a 100X oil-immersion

objective lens (N.A. = 1.3, Fluar, Carl Zeiss MicroImaging, Inc. Thornwood, NY) which was mounted in an inverted microscope (Olympus IX81, Olympus America Inc., Center Valley, PA). Laser power was measured by a power meter (PowerMax 500D, Molectron Detector Inc. Portland, Oregon) before laser beam entered the objective lens. The power switch of the laser beam was controlled by an electrical-motorized shutter (Edmund Optics Inc. Barrington, NJ). A built-in piezoelectric step motor in the microscope controlled the vertical position of the laser focal point. The glass bottom dish containing cultured HEK cells was mounted on the stage of the microscope, and the horizontal movement of stage was actuated by two perpendicularly placed step motors (Newport Inc. Irvine, CA) with a moving resolution of 50 nm. The optoporation process was monitored *in situ* by a charge-coupled device (CCD) camera (Q-imaging; Rolera-XR; Q-16467). To find the position of laser focal point, we tuned the laser to very low energy (about 3 mW) and shot the laser at an empty area of the dish. A bright spot indicating the position of laser focal point was noted on the moniter connected to the CCD camera. A marker was used to label the center of the bright spot – the focal point. Before laser optoporation, the specific area of the targeted cell was moved to the center of laser focal point. The desired laser power for optoporation of the HEK cell membrane was selected by rotating the laser beam attenuator as measured by the laser power meter. The laser exposure time of the cell was selected by programming open duration of the mechanical shutter. The term ‘targeted cell’ in this paper refers to single

HEK cells at the corners of each square grid. Cells adjacent to the targeted cells were not treated by the laser and served as the control population (Refer figure 1b,c).

4.2.3 Optoporation using femtosecond laser

SYTOX® Green nucleic acid stain (10 μM, Invitrogen, Carlsbad, CA) was added to the culture medium before each optimization experiment. Targeted cells were irradiated with varying laser parameters. An optical attenuator was used to adjust the laser average power in a range of 10 mW to 100 mW with 10 mW increments. The exposure time was varied from 10 ms to 100 ms with 10 ms increments. Targeted cells were re-located using the square grid and fluorescence signal was monitored for 1 hour after irradiation. Viability of the cells after laser exposure was determined by staining the non-viable cells with 0.5% Trypan Blue (Sigma-Aldrich), 40 minutes post-laser-treatment. For each condition, 3 or more different cells were tested.

For the transfection experiments, plasmid DNA pEGFP-N1 (9 μg/mL, 4.7kb, molar mass 2.9 MDa, Clontech, Mountain View, CA) was added to the culture medium and the cells were irradiated at 60 mW for 35 ms. Targeted cells were imaged after 24-48 hours of incubation using Nikon Eclipse TE2000-S microscope equipped with a FITC HyQ filter (Chroma Technology, Bellows Falls, VT). The images of fluorescent cells were photographed using NIS-Elements BR software version 3.0 (Nikon Instruments, Melville, NY) with the

exposure of 3 seconds and the gain of 1.00X. The cells without laser irradiation were used as negative controls to assess the background auto-fluorescence.

4.3 Results and discussion

4.3.1 Cell survival with varying laser parameters

The average laser power that can be used in the femtosecond laser optoporation experiments is critical and must be determined in advance. In general, the average laser power should be in a range that is low enough to avoid the cell damage but sufficient to induce perforation on the plasma membrane. The laser power and the exposure time at the threshold of the cell damage vary from one cell line to another. We tested the viability of HEK cells after laser irradiations at varying parameters to estimate the range of the laser power and the exposure time that the cells can tolerate. We used both direct physical observation of their morphology and differential staining using Trypan blue to access the viabilities of laser-treated cells. Cells were permanently damaged and died immediately after laser exposures at higher than 70 mW, even if they are irradiated for a very short time (Figure 2a). For the power range between 50-70 mW, the cells died only when the exposure time exceeded 50 ms. When the average laser power was set to 40-50 mW, some cellular morphological changes were observed such as membrane blebbing (“bubbles”) with the exposure time exceeding 50 ms. However, when the laser irradiation time was reduced to the range of 20-40 ms, the temporary membrane blebbing

healed shortly after the treatment and the irradiated cells survived (Figure 2b). When the laser average power was reduced to less than 20 mW, no cellular change was observed even after a very long exposure time (100 ms).

4.3.2 Optimization of laser conditions for cellular optoporation

We further optimized the parameters for cellular optoporation by monitoring the influx of a fluorescent indicator into the targeted cells. A 4 x 4 suare grid was fabricated on the bottom-sidde (outside) of the growth area (see Materials and Methods for details) to systemetically compare multiple combinations of laser power and exposure time. Single HEK cells at the corners of each square grid were identified as targeted cells and cells adjacent to the targeted cells served as the control population. Cells were irradiated with varying exposure parameters in the presence of SYTOX Green reagent. SYTOX is a small molecule-based dye which is impermeable to the intact plasma membrane of live cells. Upon entering the cells, the dye binds to nucleic acids and produce fluorescence signal. The optimal and most reproducible results were obtained from the laser exposures at 60 mV for 35 ms. As shown in Figure 3, an increase of fluorescence inside the cell was observed as a function of time, indicating successful perforation of the plasma membrane. The SYTOX dye mainly accumulated in the nucleus as expected.

As control, no sign of dye uptake was observed by the adjacent non-treated cells, indicating that the laser exposure on the plasma membrane is

reqired to change the membrane permeability. Also, no change was observed when the laser focus was in the vicinity of the cell but not on the cell. The cells were negative to the Trypan blue stain which verifies the recovery of membrane integrity and overall cell viability after laser treatment.

Another often neglected experimental parameter is the location of laser focus on the cell-membrane. Force mapping using atomic force microscope (AFM) have demonstrated significant differences in properties of protruding and stable edges of 3T3 fibroblasts in culture [155]. Active edges of 3T3 cells are flatter (average heights = 0.4–0.8 mm) and are softer (elastic modulus = 4 kPa), while stable edges are thicker (average height = 2 mm) and stiffer (elastic modulus = 12 kPa). Optoporation experiments in this work also demonstrate differences in the protruding and stable edges of HEK cells in culture (Figure 4c). Successful optoporation was achieved on the protruding edge of the cells using 60 mW laser power and 35 ms exposure time, however, the power had to be increased to 70 mW to achieve optoporation of stable edges of HEK cells. This underscores the significance of choosing specific location on cell membrane while conducting optoporation experiments.

When the laser exposure time was decreased to 30 ms, the influx of SYTOX into the targeted cells was observed, however the intensity of the fluorescence (Figure 4d) was decreased compared to figure 3f. This result

indicates that the total amount of dye introduced into the cell was reduced at the exposure time of 30 ms compared to 35 ms.

We then increased the exposure time to 40 ms at laser power at 60 mW), membrane blebbing was observed within the target region indicating some cell damage (Figure 5). In most cases, when 2 or more bubbles are present for longer than 10 min post-exposure, the cell membrane is compromised based on the Trypan blue staining. However, when the size of the bubble is about 1 micrometer or less in diameter, most cells recover within 10 min of laser treatment with no signs of membrane damage. A summary of results are shown in Figure 6.

4.3.3 Transfection of HEK cells by femtosecond laser-asisted cellular optoporation

We used the optimized laser paremeter (laser power = 60 mW; exposure time = 35 ms) to perform DNA transfection experiments with HEK cells. Cells were irradiated in the presence of plasmid DNA pEGFP-N1 in the culture medium and then returned to the incubator. Targeted cells were identified by using the grid as described in the methods section 24-48 hours post-treatment. Positive expression of GFP in the irradiated cells and their daughter cellls after cell division indicates that the plasmid DNA was successfully introduced into the cell interior by optoporation treatment (Figure 7). No fluorescence was observed in the surrounding cells not exposed to the laser.

4.4 Conclusions

In this work, we used both a membrane impermeable fluorescent dye and a plasmid DNA carrying the coding sequence for green fluorescent protein (GFP) to analyze the entry of extrinsic molecules into the target cells. We simulated the near infrared (NIR) femtosecond laser ablation process and demonstrated that the transient perforation produced by the process can be smaller than the size of the laser focal volume. The standardization of laser parameters should result in more reproducible results for any particular cell line.

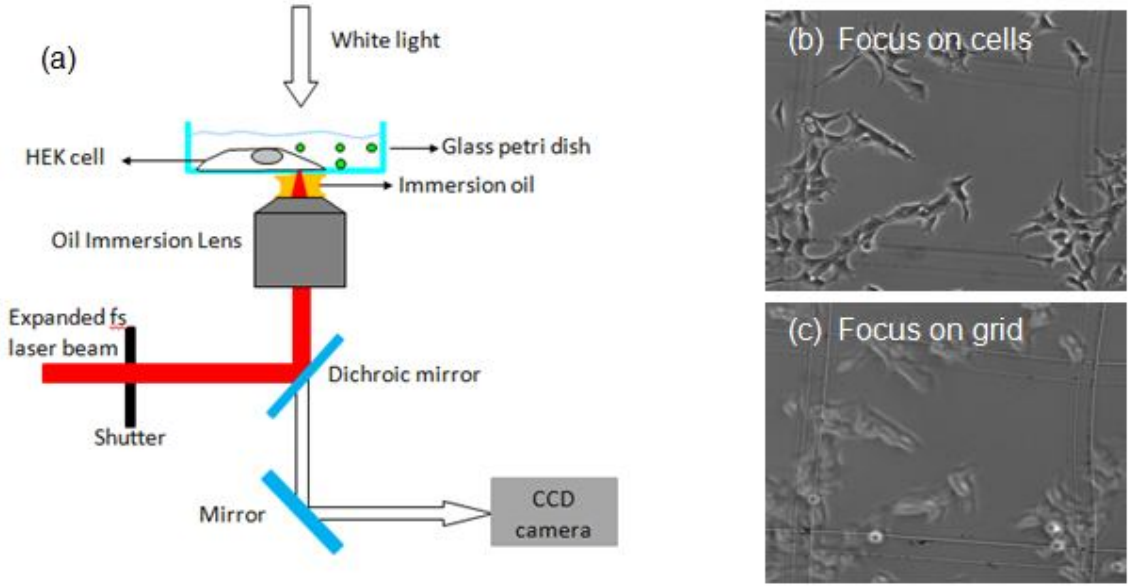

Figure 4.1 Schematic laser setup for optoporation

(a) Schematic representation of the laser set-up for opto-poration of targeted single HEK cell. (b) A grid was fabricated by a tungsten carbide scriber on the under-side of a glass-bottom culture dish. HEK cells were then seeded and grown to approximately 10-30% confluency. HEK cells in focus on the top side of the culture chamber. (c) Grid in focus on the underside of the culture dish.

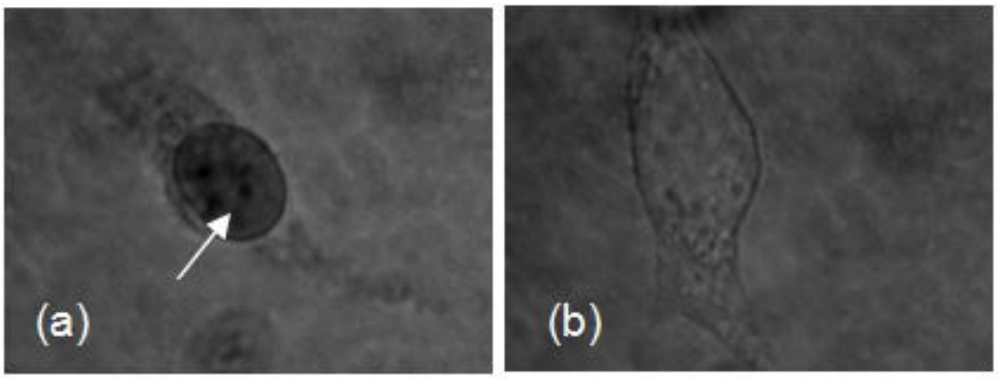

Figure 4.2 Bright field images of laser treated HEK cells: Trypan Blue (0.5%) was added to the culture medium 40 minutes after laser treatment to test cell-viability. Trypan Blue is a membrane-impermeable differential dye that stains dead cells but not live cells.

(a) High laser exposure (power = 80 mW; exposure time = 10 ms) on targeted HEK cell stained with Trypan blue. Presence of trypan blue indicates that the integrity of the HEK plasma membrane has been compromised. (White arrow) (b) HEK cell survive after optimal laser exposure (power = 60 mW; exposure time = 30 ms).

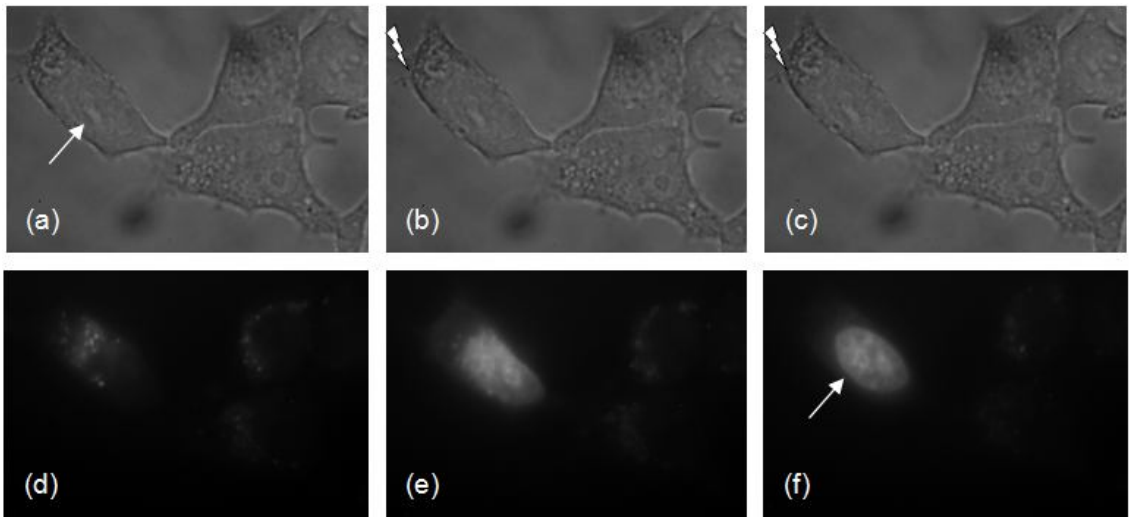

Figure 4.3 Bright field images (a, b, c) and fluorescence images (d,e,f) of intact HEK cells optoporation experiment in the presence of SYTOX dye.

The position of the laser focal spot is marked by the lightning symbol. White arrow points to the targeted cell. Laser power = 60 mW; Exposure time = 35 ms. (a)(d) Before laser irradiation; (b)(e) Fluorescence is observed inside the HEK cell 10 min after laser optoporation; (c)(f) Syrox labels only the nucleus of the cell, which can be clearly seen in the figure, 20 min after optoporation.

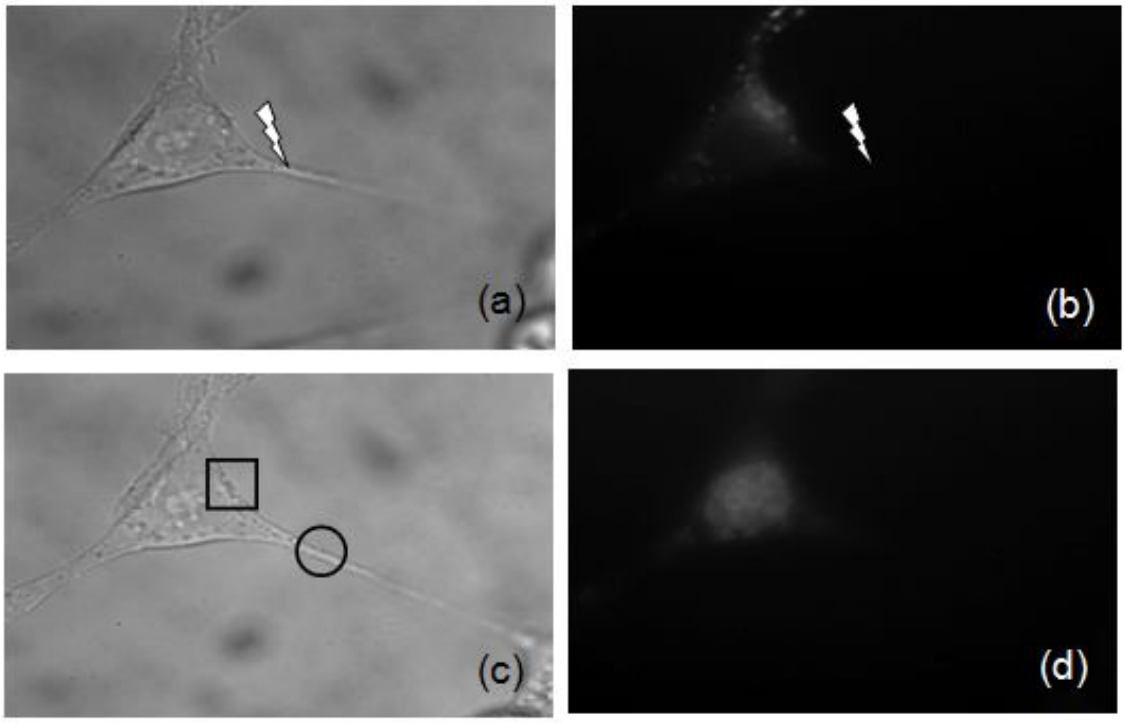

Figure 4.4 Bright field (a,c) and fluorescence images (b,d) of an HEK cells after laser treatment in the presence of SYTOX dye.

The position of the laser focal spot is marked by the lightning symbol. (laser power = 60 mW; exposure time = 30 ms) (a,b) 10 min post-exposure (c,d) 20 min post-exposure. Fluorescence labeling the nucleus was observed 20 min after laser optoporation. Square in (c) = stable edge; circle in (c) = protruding edge

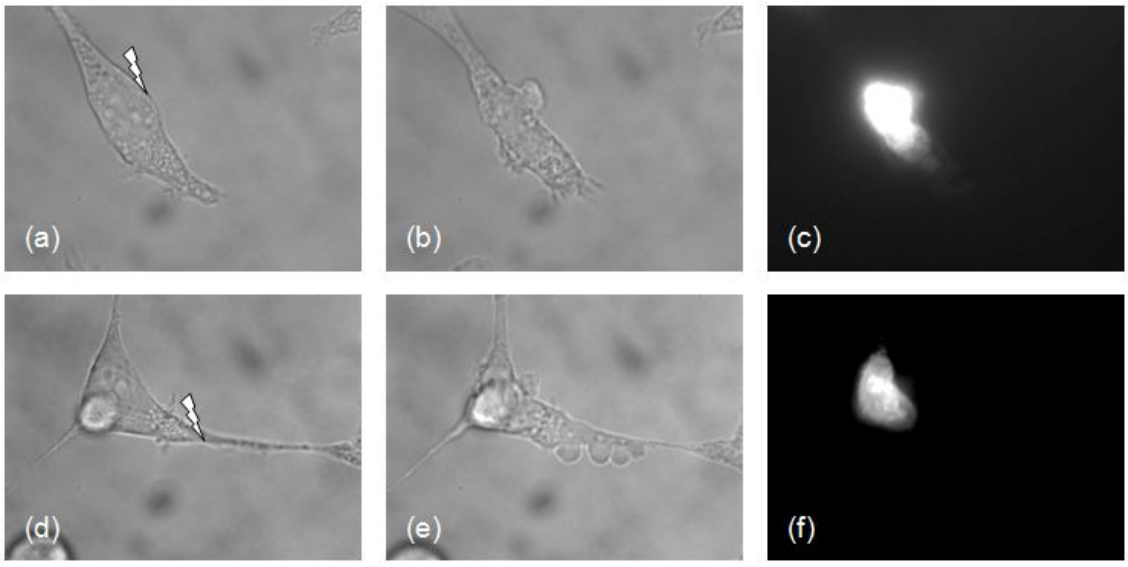

Figure 4.5 Morphological changes of two HEK cells (laser power = 60 mW; exposure time = 40ms) post-irradiation at the marked positions

(a,d) 0 min after laser treatment; (b,e) 10 min after laser treatment. Excessive local swelling of the plasma membrane was observed in both cells. (c,f) 20 min after laser treatment. SYTOX dye is seen inside the cell, however it does not bind to only the nucleus. Both the cells were determined to be non-viable based on Trypan blue staining.

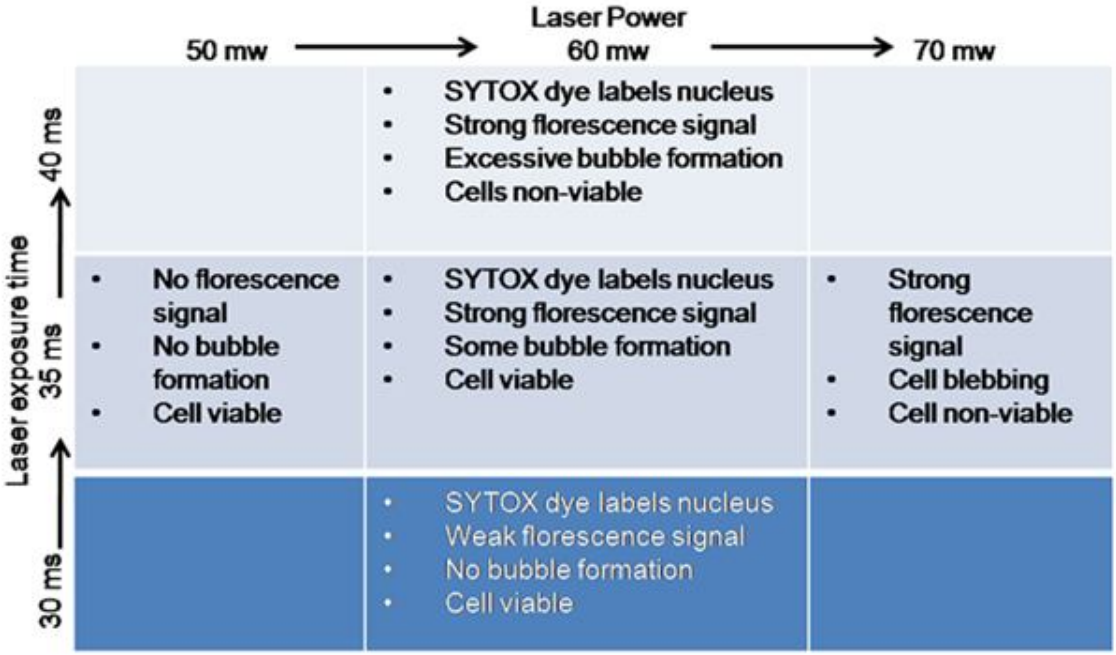

Figure 4.6 Summary of femtosecond-optoporation results using HEK cell line

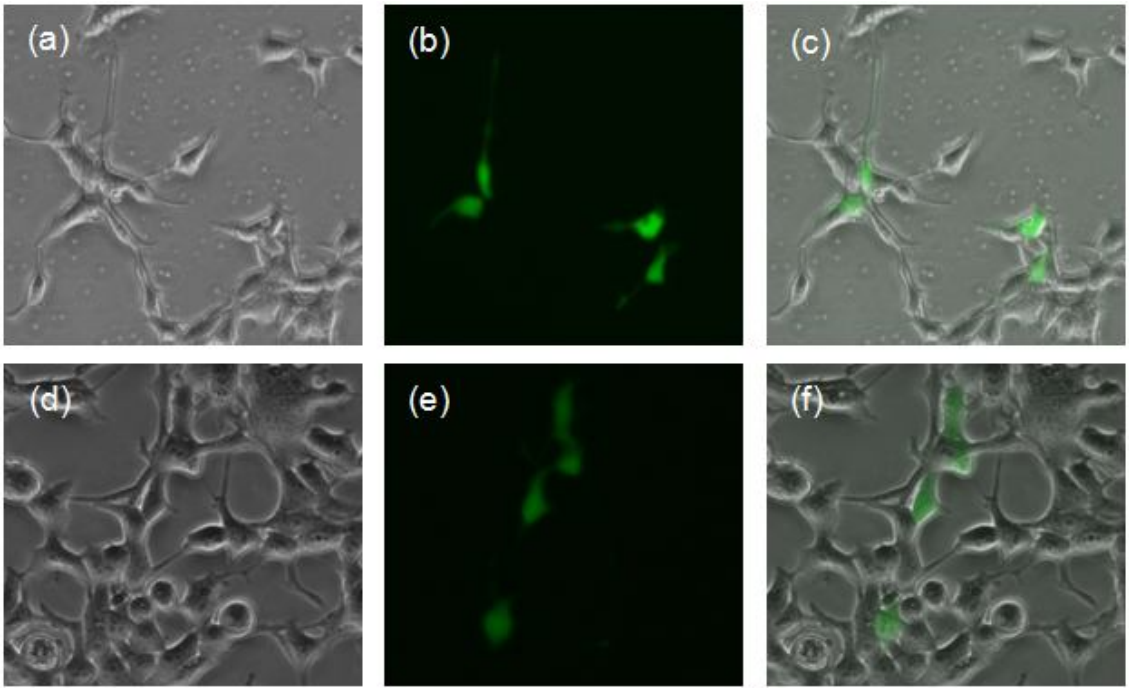

Figure 4.7 HEK cell transfection using femtosecond laser

Four HEK cells were optically transfected with plasmid DNA pEGFP-N1. (a,c) Brightfield images. (b,e) Florescence images. (c,f) Superimposed images.

Chapter 4, in part, is a reprint of material that is published as: Soman P*, Zhang W*, Umeda A, Zhang Z, Chen S. Femtosecond Laser-Assisted Optoporation for Drug and Gene Delivery into Single Mammalian Cells. Journal of Biomedical Nanotechnology 2011; 7 (3): 334-41 *Shared first author

CHAPTER FIVE:

Integrated two-photon polymerization with nanoimprinting for direct digital nanomanufacturing

5.1 Introduction

Nanoimprint lithography (NIL) techniques have been regarded as parallel nanofabrication methods for high-resolution and high-aspect-ratio features [156-162]. NIL has the potential to significantly impact many applications in areas including photonic crystals for high-brightness LEDs, biochemical sensors, and large format display polarizers [163-165]. To successfully imprint nanostructures using NIL, a rigid mold capable of nano-patterning thermal or photo-curable materials over a large area with high accuracy and repeatability is crucial. Unfortunately, fabricating nanoimprinting molds in silicon or quartz, the two most commonly used materials, usually requires costly and often unavailable cleanroom equipment and time-consuming steps, including e-beam lithography (EBL) and reactive ion etching (RIE) [166-169]. A recent development is to make multiple polymer molds from a single master-silicon or -quartz mold to save time and cost. Polymer molds have desirable and easily tunable bulk and surface properties that are well-suited for the nanoimprinting process [170, 171]. However, because this fabrication process requires a master mold, the whole process is still costly and time-consuming.

In this paper, we demonstrate the plausibility of creating a low-cost polymer nanoimprinting mold by using the two-photon polymerization (TPP) technique, which avoids the need of making silicon or quartz molds entirely. TPP induced by femtosecond laser irradiation in photopolymers has been demonstrated for its ability to fabricate intricate nanoscale structures [172, 173].

During TPP, the photopolymer simultaneously absorbs two photons to activate the chain reaction of polymerization. Only the central portion of the laser beam with high energy intensity is able to induce such two-photon absorption, due to the Gaussian distribution of the energy intensity over the laser beam cross section. Therefore, TPP is able to break the diffraction limit which restrains the resolution of photo-polymerization fabrication. Sub-100 nm features have already been successfully fabricated by TPP [174]. The advantages of TPP over EBL include the low cost for capital equipment and TPP's virtual absence of any proximity effect which restrains the distance that structures can be placed from each other through the EBL process [175].

Despite its many advantages, TPP is an extremely slow serial (point-by-point) fabrication process, which has precluded it from being used in the mass production of nanostructures[176-178]. This work, by using TPP to make reusable nanoimprinting molds, indirectly enables the utilization of TPP in mass production. The TPP technique does not require costly cleanroom facilities or time-consuming processes, thus costing less than the traditional mold-fabrication methods. Moreover, a variety of polymers can be used to make such molds, which ensures that it is relatively easy to obtain the desirable bulk and surface properties for polymer molds suitable for different imprinting projects.

Poly (ethylene glycol) diacrylate (PEGDA) was patterned in our study to demonstrate the imprinting capacity of the polymer molds made by TPP. PEGDA is a Food and Drug Administration (FDA) approved, PEG-based

hydrogel that has been widely utilized in the fabrication of tissue-engineering scaffolds with microscale structures [179, 180]. However, research efforts to make nanoscale structures in tissue engineering scaffolds using PEGDA have been relatively lacking, despite of the fact that the *in vivo* stimuli of cells are in nanoscale [27, 181-184]. This work will bridge this gap by transferring nanostructures into PEGDA through a polymer mold.

5.2 Materials and methods

5.2.1 Material preparation for TPP

The photopolymer we used for the TPP fabrication was dipentaerythritol pentaacrylate (DPPA, Sartomer Inc., Exton, PA), used as received. We chose this acrylic polymer based on several considerations. First, DPPA is fast curing, as a result of the existence of five acrylate groups in each of its molecules. Second, its abrasion resistance and flexibility with hardness characteristics make it a very suitable material for molds. Third, DPPA has one hydroxyl group in each molecule, so a fluorosilane layer, which promotes releasing in the imprinting process, can covalently bond onto its surface.

To increase the TPP rate of DPPA, 1% photoinitiator (Irgacure 819, Ciba Specialty Chemicals, Tarrytown, NY) was thoroughly mixed with DPPA by heating the mixture in 80 °C silicone oil (Fisher Scientific Inc., Pittsburgh, PA). To activate the chain reaction of TPP, the photopolymer must simultaneously absorb two photons, whose effect is equivalent to absorbing a single photon of half the wavelength. Besides, the photopolymer must be transparent to the

laser beam to eliminate single photon polymerization which may reduce the fabrication resolution. Therefore, a suitable photopolymer for TPP induced by an 800 nm laser should have high absorption at 400 nm and negligible absorption at 800 nm. To verify that DPPA with 1% photoinitiator is such a suitable photopolymer, the absorption spectra of DPPA with 1% photoinitiator and 0% photoinitiator, respectively, were measured by a spectrophotometer (Cary 5000 UV-Vis-NIR, Varian, Inc., Palo Alto, CA). As Figure 1 shows, DPPA with 1% photoinitiator had a high absorption rate at a wavelength of 400 nm, a fact apparently attributable to the photoinitiator because DPPA with 0% photoinitiator did not exhibit such a strong absorption rate at 400 nm. In addition, both DPPA with 1% and 0% photoinitiator had no natural absorption at the spectral region near 800 nm, which demonstrated that the single photon polymerization could not occur in these materials under near infrared (NIR) femtosecond laser irradiation.

The DPPA structures produced by TPP need to adhere onto a glass substrate--the mold substrate--during the TPP process in order to be used as the imprinting mold. The mold substrates (Fisher Scientific Inc., Pittsburgh, PA) were cleaned for 8 minutes in piranha solution consisting of a 2:1 mixture of sulfuric acid and hydrogen peroxide, washed by deionized (DI) water, and dried by high-pressure nitrogen. To enhance the adhesion with DPPA, the substrates were then treated for 5 minutes in a 1-mM solution of 3-trichlorosilyl propyl methacrylate (TPM, Fluka Chemicals, Milwaukee, WI) in a 4:1 mixture of

heptane (Fisher Scientific Inc., Pittsburgh, PA) and carbon tetrachloride (Sigma-Aldrich Inc., Milwaukee, WI). Subsequently, the substrates were washed by carbon tetrachloride and dried by nitrogen. Finally, in order to get rid of the chlorhydric acid generated in the previous step and the residual water on the surface, the substrates were soaked in DI water for 2 minutes and then baked on a hot plate (Super-Nuova, Barnstead Thermolyne Corporation, Dubuque, IA) at 100 °C for 5 minutes.

5.2.2 TPP fabrication process

Figure 2 shows the experimental setup for TPP fabrication. The excitation source for TPP was a Ti:sapphire femtosecond laser (Vitesse, Coherent Inc., Santa Clara, CA) producing 100-femtosecond duration pulses with a central wavelength of 800 nm at a repetition rate of 80 MHz. The laser beam was expanded by a 2X beam expander to overfill the incidence aperture of a 100X oil-immersion objective lens (N.A. = 1.3, Fluar, Carl Zeiss MicroImaging, Inc., Thornwood, NY) which focused the laser beam into the volume of DPPA. The laser power employed for the fabrication was 5 mW, measured by a power meter (PowerMax 500D, Molectron Detector Inc., Portland, Oregon) before the laser beam entered the objective lens. The power switch of the laser beam was controlled by an electrical-motorized shutter (Edmund Optics Inc., Barrington, NJ). The vertical position of the laser focal point was controlled by the movement of a vertically-mounted step-motor (Newport Inc., Irvine, CA). The fabrication process was monitored *in situ* by a

charge-coupled device (CCD) camera (CV-S3200, JAI Inc., San Jose, CA). The mold structures were generated by moving a motorized stage (Newport Inc., Irvine, CA), which held the glass substrate, at a speed of 50 μm/second.

5.2.3 Post-treatment of the mold

Within 5 minutes of being fabricated by TPP, the mold was developed in ethanol (Decon Labs Inc., King of Prussia, PA) for 3 minutes to wash away uncured photopolymer. After the development process, there were still some residual acrylate groups on the surface of the mold that might bond with the imprinted material and hinder mold detachment. To remove these acrylate groups, the mold was then soaked in a solution of 1% photoinitiator (Irgacure 2959, Ciba Specialty Chemicals, Tarrytown, NY) in DI water and was irradiated with a UV lamp (OmniCure S2000, Exfo Life Sciences & Industrial Division, Mississauga, Ontario, Canada) for 2 minutes.

To facilitate detachment of the mold during the imprinting process, it was crucial to grow a releasing layer on the mold surface. Fluorosilane was chosen as our releasing-layer material because it is highly hydrophobic, as a result of its low surface energy. Figure 3 shows the schema of the silanization process. First, two glass petri dishes, containing several drops of silicon tetrachloride and the mold, respectively, were placed in a vacuum oven (Isotemp Vacuum Oven Model 280A, Fisher Scientific Inc., Pittsburgh, PA) for 2 hours. During this process, a layer of silicon tetrachloride (Acros Organics, Morris Plains, NJ) was grown on the mold surface, as Figure 3 (a) illustrates. Then the mold was

soaked in DI water for 2 minutes, during which time the chlorine ions of silicon tetrachloride were replaced by hydroxyl groups of water molecules, as Figure 3 (b) shows. This replacement greatly increased the number of hydroxyl groups on the mold surface, making it easier for fluorosilane molecules to bond onto it. After that, the mold was baked on a hot plate at 100 °C for 10 minutes to strengthen the newly formed layer of hydroxyl groups by forming -Si-O-Si- bonds between adjacent silicon tetrachloride molecules, as illustrated in Figure 3 (c). Next, a layer of fluorosilane -- tridecafluoro-1,1,2,2-tetrahydrooctyl-1 trichlorosilane (TFTT, United Chemical Technologies Inc., Bristol, PA) was grown on the mold surface following similar steps as the ones used for growing silicon tetrachloride, with the only difference being that TFTT, instead of silicon tetrachloride, was placed onto one of the two glass petri dishes. Finally, the mold was again soaked in DI water for 2 minutes and baked on a hot plate at 100 °C for 10 minutes. Figure 3 (e) and (f) illustrate the reactions that occurred in those two steps. After the fluorosilane had been successfully grown on the mold, the mold was stored in a vacuum desiccator (Desi-Vac, Fisher Scientific Inc., Pittsburgh, PA).

5.2.4 Imprinting in PEGDA

The imprinting process was conducted in a mask aligner (SUSS MA-6, SuSS Microtech, Munich, Germany), following the procedure outlined below. The procedure is discussed in detail in Ref [185]. Firstly, PEGDA (MW 258, Sigma-Aldrich Inc., Milwaukee, WI) was thoroughly mixed with 1% Irgacure

2959 through 5-minute sonication (Branson Ultrasonics Corporation, Danbury, CT) to increase its cross-linking rate. The glass sample substrate was treated with TPM to improve its adhesion with PEGDA, following the same procedure as the one used to treat the mold substrate during the material-preparation stage. Next, the mold was secured on the sample stage of the mask aligner by two strips of 100-μm-thick sticky tapes. The sample substrate that served as a transparent dummy mask was similarly affixed onto a glass dummy plate by two sticky tapes. The tapes on the mold and the sample substrate also served as spacers that protected the mold from being damaged during the imprinting process by preventing their direct contact with each other. Subsequently, the glass dummy plate with the sample substrate affixed on it was mounted to the mask holder of the mask aligner by vacuum suction so that the glass substrate was directly above and facing the mold. Lastly, a drop of PEGDA was deposited on the mold surface by a glass pipette. The sample stage was then lifted upwards until the tapes on the mold and on the sample substrate contacted each other. Due to the mold's hydrophobic surface, PEGDA could not immediately fill in the nanoscale structures on the mold immediately after the contact, so it was allowed to spread for 3 minutes before the application of UV irradiation. PEGDA was then irradiated by 365 nm UV light for 30 seconds. After the exposure, the mold was detached from the sample substrate by the automatic descent of the sample stage. After the imprinting process, the mold was taken from the sample stage and could be used in subsequent imprinting processes without any further surface treatment.

5.3 Results and discussion

A scanning electron microscope (SEM, Supra 40VP, Zeiss, Carl Zeiss SMT Inc., Peabody, MA) was employed to examine the mold and the PEGDA structures obtained by the imprinting process. The parallel lines--the patterns of the mold--remained intact and firmly attached to the mold substrate after having completed multiple imprinting processes, as figure 4 (a) shows. The width and height of each line is 400 nm and 1.2 μm, respectively, and the distance between adjacent lines is 5 μm. The width and depth of the structures fabricated by TPP is determined by the laser power, the laser scanning speed, the concentration of photoinitiator in photopolymer, and the molecular structure of photopolymer. Figure 4 (b) presents a side view of the parallel lines and provides a direct view of the height of the lines. Figure 4 (c) and (d) show that the imprinted PEGDA structures consist of parallel trenches of the same dimensions and spacing as the parallel lines on the mold, thus demonstrating that our imprinting process accurately transferred the patterns on the DPPA mold to PEGDA over a large area. While the widths and the spacing of the trenches can be easily measured from the top-view SEM image on Figure 4 (c), the height of the trench cannot be obtained that way. Nor can it be obtained by an atomic force microscope (AFM) scan because the trench is too narrow for the AFM tip to approach. Therefore, to measure the height of the trenches, the cross-sectional view of the trenches, as shown by Figure 4 (d) was needed. The trenches were perpendicularly cut by a scalpel to expose their cross section. Because cutting on bare PEGDA surface will generate debris near the cut that

may obstruct the cross-sectional view of the trench, a 6 nm-thick layer of Pt/Pd alloy was deposited on the PEGDA surface before cutting to prevent debris.

Our work demonstrates that imprinting molds made by TPP could successfully transfer nanoscale patterns to photo-curable hydrogel—PEGDA. In order to pattern PEGDA in mass production with high fidelity, the mold must be able to detach easily and completely from the imprinted sample with no residual PEGDA left on it after each imprinting. This goal was achieved in our work by the pre-treatment of the mold substrate that enhances its adhesion with DPPA and by the post-treatment of the mold which prevents its adhesion with PEGDA during the imprinting process. During the post-treatment of the mold, to facilitate the detachment of the mold from the imprinted structures, it was crucial to grow a layer of silicon tetrachloride on the mold surface before growing the releasing layer of fluorosilane. This is because silicon tetrachloride tripled the number of hydroxyl groups on the mold surface so that a much denser layer of fluorosilane was able to bond onto it. Whitesides et al. reported another method to increase the number of hydroxyl groups on the polymer surface by transforming some methyl groups of the polymer to hydroxyl groups via RIE [186]. This technique promises to be an alternative for the post-treatment of the polymer mold surface since it is simpler than the silicon tetrachloride treatment used in our experiment.

Our TPP imprinting technique could be used to make nanoimprinting molds from a variety of materials. Most acrylic photopolymers whose surface

properties could be modified by the post-treatments can be patterned by TPP to create nanoimprinting molds. Moreover, some fluoro-based polymers such as perfluoropolyether (PFPE) have intrinsic ultralow surface energy, as a result of which molds made of such materials have inherent anti-attaching ability so they can imprint without any surface treatment. Previous studies have demonstrated the superior imprinting capability of PFPE nanoimprinting molds made from a master silicon mold by UV polymerization [187, 188]. We purpose that PFPE can also be patterned by TPP to make nanoimprinting molds, which will further simplify the fabrication procedures depicted in this paper.

5.4 Conclusions

A polymer nanoimprinting mold was created by the femtosecond laser induced TPP. Because the etching step is removed from the mold fabrication process and no costly EBL facility is employed, TPP method is faster, easier, and less costly than the fabrication processes using the traditional silicon or quartz molds. The mold was treated with a series of silanization processes to facilitate the detachment of the mold from the imprinted materials. PEGDA was patterned by the mold to demonstrate its imprinting capacity. The SEM images of the mold and the imprinted PEGDA patterns show that a group of 400 nm-wide parallel lines were successfully transferred to PEGDA with high accuracy over a large area, thus demonstrating the feasibility of making nanoimprinting molds by TPP. More intricate nanoimprinting molds can be made by the TPP technique because it is relatively easy for TPP to create smaller features with

arbitrary geometry. We believe the integration of TPP with NIL will significantly reduce the cost and time-to-production for direct, digital nanomanufacturing.

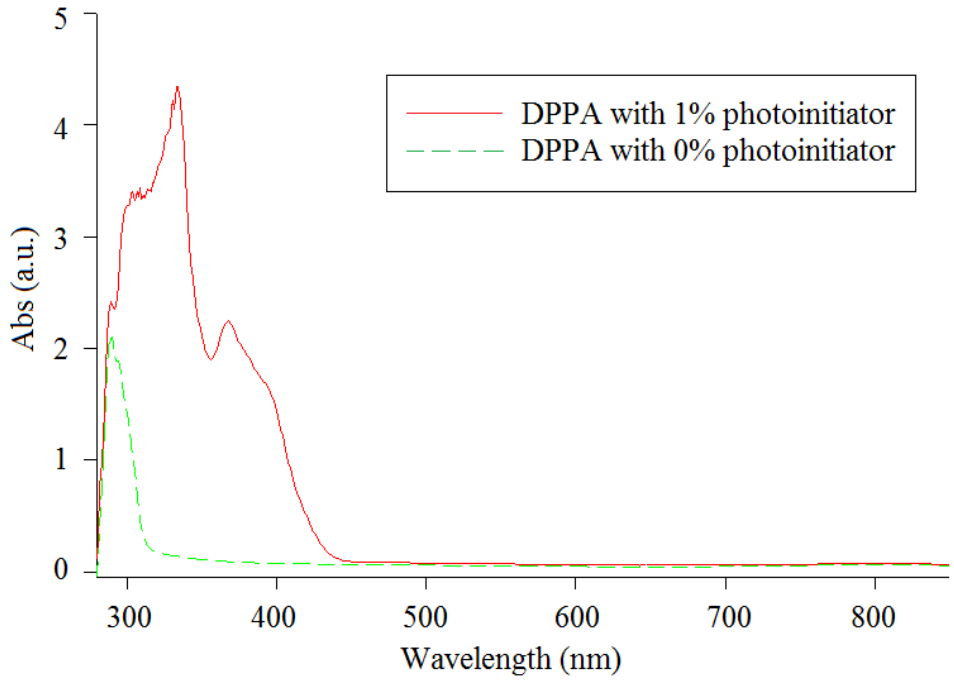

Figure 5.1 Absorption spectra of DPPA with 1% photoinitiator and with 0% photoinitiator

There is no absorption near 800 nm in either solution and there is strong absorption in DPPA with 1% photoinitiator near 400 nm.

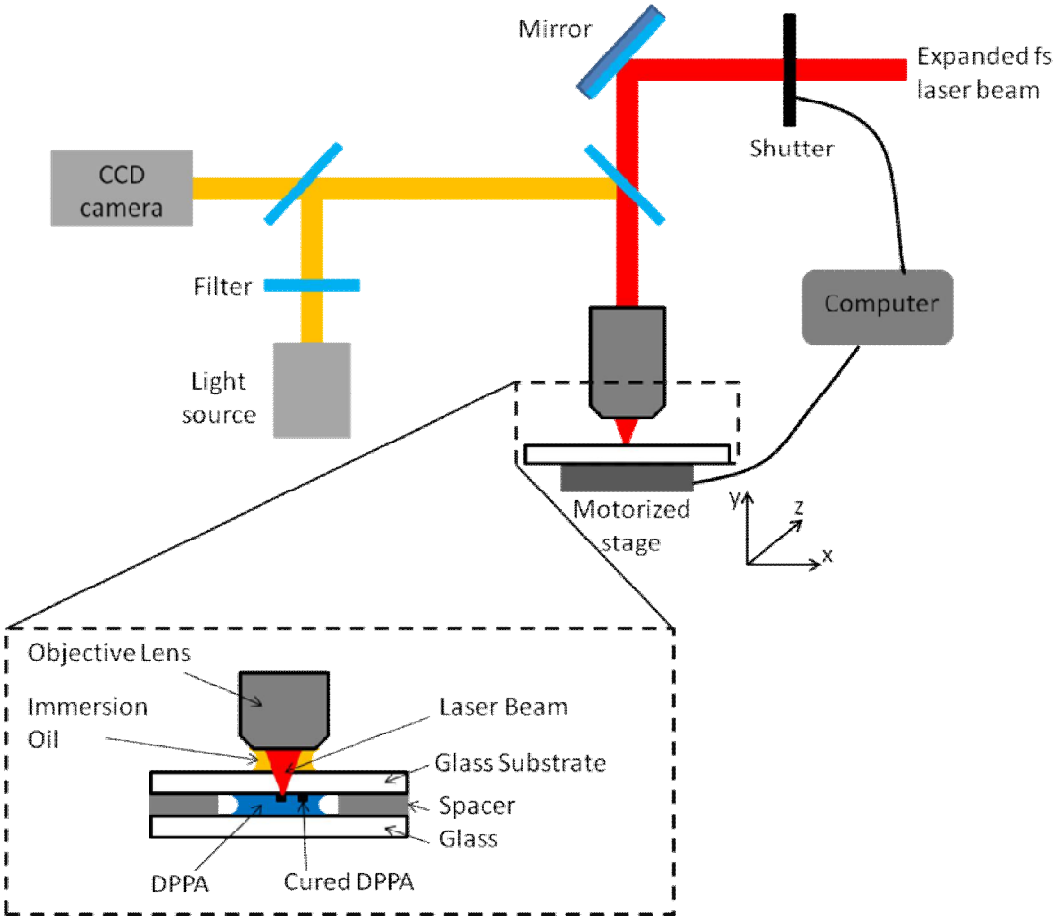

Figure 5.2 Experimental setup of two-photon polymerization

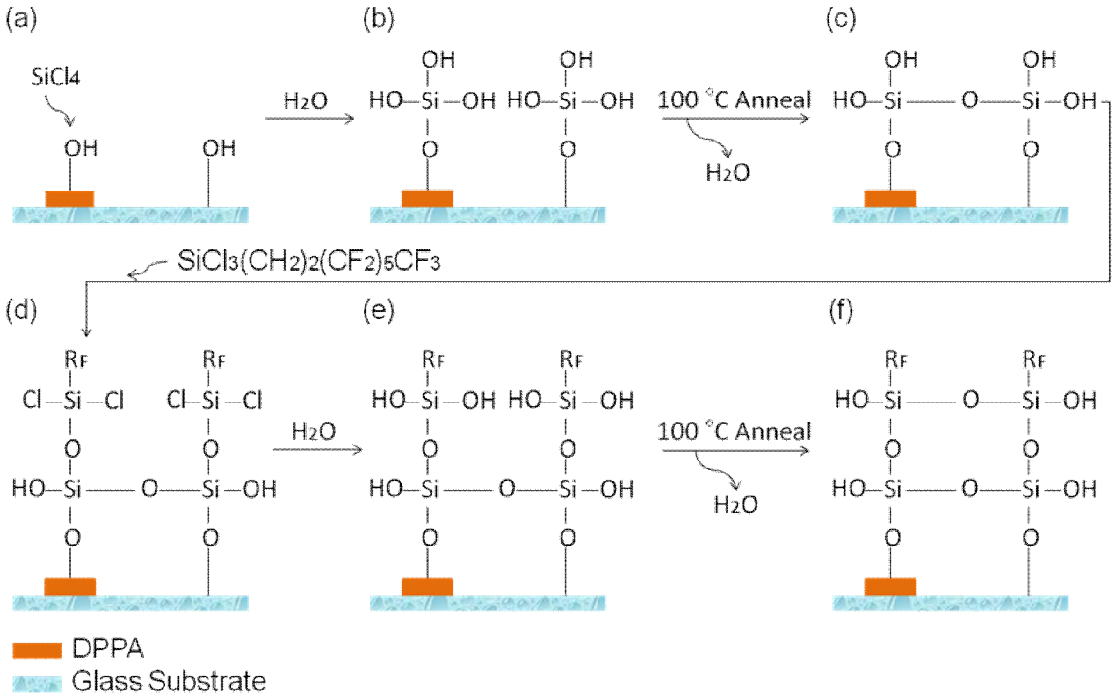

Figure 5.3 Schematic diagram of the post-treatment of the mold surface

(a) silicon tetrachloride reacted with the hydroxyl groups on the mold surface; (b) the mold was soaked in DI water and the number of hydroxyl groups on the mold surface greatly increased as the chlorine ions of silicon tetrachloride were replaced by hydroxyl groups in water molecules; (c) the mold was annealed on a hot plate at 100 °C to stabilize the layer of hydroxyl groups by forming -Si-O-Si- bonds between adjacent silicon tetrachloride molecules; (d) tridecafluoro-1,1,2,2-tetrahydrooctyl-1 trichlorosilane reacted with the hydroxyl groups on the mold surface, RF = (CH2)2(CF2)5CF3; (e) the mold was once again soaked in DI water; (f) the mold was annealed on a hot plate at 100 °C.

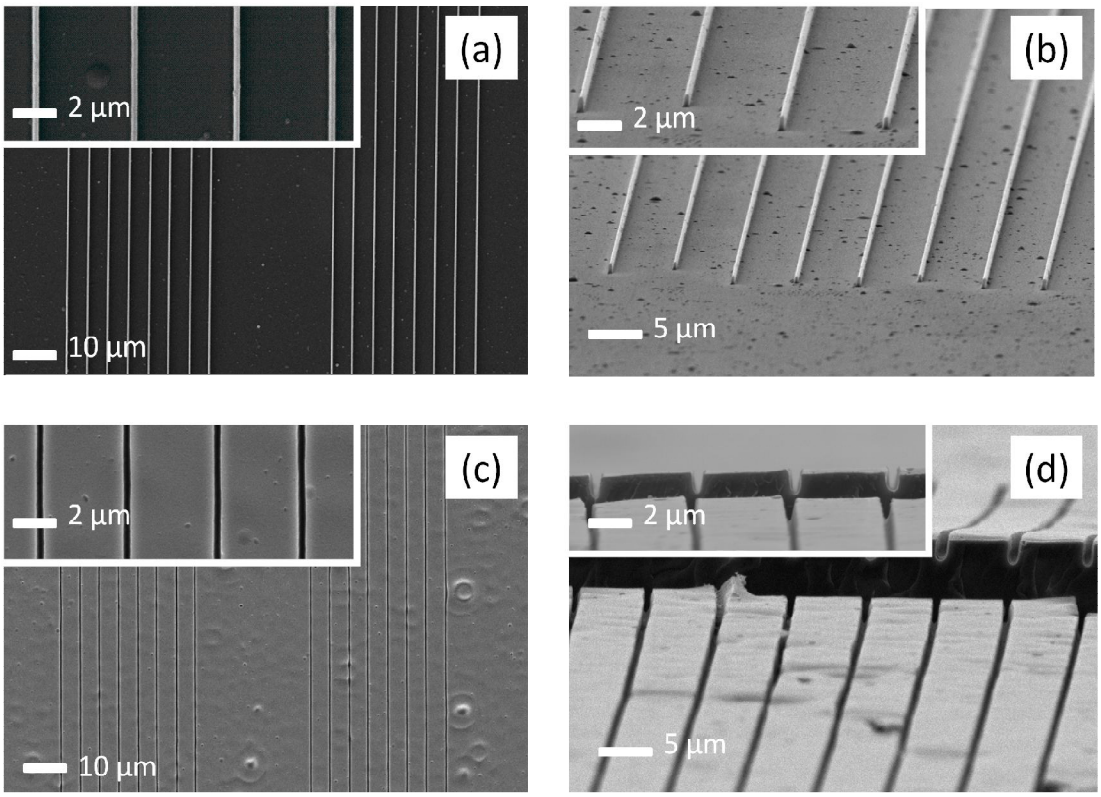

Figure 5.4 SEM images of the imprinted PEGDA structures and the DPPA mold after imprinting

(a) DPPA mold of 400 nm-wide lines with a pitch of 5 μm, (b) side view of the DPPA mold, (c) imprinted PEGDA structures of 400 nm-wide trenches with a pitch of 5 μm, (d) perspective view of the PEGDA trench cross section; the inset is the vertical view of the trench cross section.

Chapter 5, in part, is a reprint of material that is published as: Zhang W, Han L-H, Chen S. Integrated Two-Photon Polymerization with Nanoimprinting for Direct Digital Nanomanufacturing. Journal of Manufacturing Science and Engineering 2010; 132 (3): 030907-5

CHAPTER SIX:

Summary and future work

6.1 Summary

In this thesis I have demonstrated the application of a femtosecond laser in the investigation of *in vitro* cell-environment interaction. In chapter three, femtosecond laser induced two photon polymerization was employed to develop suspended web structures which exhibit positive and negative Poisson's ratio (NPR), based on analytical models. NPR webs demonstrate biaxial expansion/compression behavior, as one or multiple cells apply local forces and move the structures. In recent years, cell response to surface rigidity has been extensively studied by modulating the elastic modulus of hydrogels. In the context of biomaterials, Poisson's ratio, another fundamental material property has been not explored, primarily because of challenges in tuning the Poisson's ratio in biological scaffolds. We also demonstrated abnormal cell division on NPR web structures.

In chapter four, focused near-infrared (NIR) femtosecond laser pulses were used to transiently perforate the cell membrane of targeted human embryonic kidney (HEK) cells and the uptake of extrinsic molecules into the targeted cells were observed. Several experimental parameters such as laser power, exposure time, and the location of laser irradiation were optimized using a membrane impermeable fluorescent dye. The optimized parameters were used to investigate the entry of a plasmid DNA carrying the coding sequence for green fluorescent protein (GFP) into the target cells. Femtosecond-assisted

optoporation combined with a lab-on-a-chip device can be potentially used in high-throughput screening of targeted cells.

In chapter five, we demonstrated the plausibility of integrating two-photon polymerization (TPP) with nanoimprinting for direct, digital nanomanufacturing. TPP offers manufacturing of nano-molds at a low cost, while the nanoimprinting process using the nano-molds enables massively parallel printing of nanostructures. A Ti:sapphire femtosecond laser (800 nm wavelength, 100 fs pulse width, at a repetition rate of 80 MHz) was used to induce TPP in dipentaerythritol pentaacrylate to fabricate the nanoimprinting mold with 400 nm wide line array on a glass substrate. The mold surface was silanized by tridecafuoro-1,1,2,2-tetrahydrooctyl-1 trichlorosilane to facilitate the detachment of the mold from the imprinted material. This mold was then used to fabricate PEGDA patterns. A spectrophotometer and a scanning electron microscope (SEM) were used to characterize the materials and nanostructures.

6.2 Future work

We have demonstrated for the first time the influence of Poisson's ratio, one of the fundamental material properties, on cell behavior. Equally importantly, we conducted the earliest research on cell response to suspended web structures. Since both research areas have not been explored before, it is a totally new territory with lots of unknowns. What we have accomplished in this thesis may just be the end of the beginning of the research in this field.

Theoretically, a large variety of cell behavior can be investigated on negative Poisson's ratio (NPR) web structures. Nevertheless, the differentiation of stem cell on NPR webs would be particularly interesting. It has been demonstrated that many properties of the underlying substrate such as the size of the pattern[189], the geometry[38], and the elasticity[47] were able to direct the stem cell differentiation, and those properties directed the fate of stem cell mechanically through the mechano-signal transduction. Therefore, it is reasonable to hypothesize that the Poisson's ratio, which also influences cell behavior through mechano-signal, may be able to direct stem cell differentiation as well.

Another application worth trying is the influence of NPR webs on the efficiency of drug and gene delivery. It was demonstrated that the phenotypic change of cells medicated by micro- or nano- featured substrates could substantially improve the transfection efficiency of nonviral gene delivery[190-195]. As we have observed in the cell experiments on NPR webs, there was interesting phenotype change of cells on the webs. Thus it is likely that the NPR webs might change the gene transfection efficiency as well.

The challenge in further research of the negative Poisson's ratio webs would be to find a suitable polymer to make the web. The PEGDA we use in the experiment is soft enough and can be easily pulled by cells, however, it does not have enough resilience to withstand the cell pulling force for an extended

time while being incubated in the 37ºC cell culture environment. In the experiment we found that the cells could significantly deform and ruin the web structure after longer than 3 days' incubation. Therefore, future work will have to first focus on testing and characterizing the suitable biomaterials. Moreover, it is easier to fabricate larger suspended web structures with high resilience polymer, so that more cells can be seeded on a single web and fewer webs are needed to generate statistically significant data, which will potentially expedite the research process.

REFERENCES:

1. Ruoslahti E,Reed Jc Anchorage dependence, integrins, and apoptosis. Cell 1994; 77 (4): 477-78

2. Gumbiner Bm Cell adhesion: The molecular basis of tissue architecture and morphogenesis. Cell 1996; 84 (3): 345-57

3. Frisch Sm,Ruoslahti E Integrins and anoikis. Curr. Opin. Cell Biol. 1997; 9 (5): 701-06

4. Fassler R,Meyer M CONSEQUENCES OF LACK OF BETA-1 INTEGRIN GENE-EXPRESSION IN MICE. Genes Dev. 1995; 9 (15): 1896-908

5. Zou Hy,Niswander L Requirement for BMP signaling in interdigital apoptosis and scale formation. Science 1996; 272 (5262): 738-41

6. Habtezion A, Toivola Dm, Asghar Mn, Kronmal Gs, Brooks Jd, Butcher Ec,Omary Mb Absence of keratin 8 confers a paradoxical microflora-dependent resistance to apoptosis in the colon. Proc. Natl. Acad. Sci. U. S. A. 2011; 108 (4): 1445-50

7. Flemming Rg, Murphy Cj, Abrams Ga, Goodman Sl,Nealey Pf Effects of synthetic micro- and nano-structured surfaces on cell behavior. Biomaterials 1999; 20 (6): 573-88

8. Nikkhah M, Edalat F, Manoucheri S,Khademhosseini A Engineering microscale topographies to control the cell-substrate interface. Biomaterials 2012; 33 (21): 5230-46

9. Kim M, Choi Jc, Jung Hr, Katz Js, Kim Mg,Doh J Addressable Micropatterning of Multiple Proteins and Cells by Microscope Projection Photolithography Based on a Protein Friendly Photoresist. Langmuir 2010; 26 (14): 12112-18

10. Lee Sh, Moon Jj,West Jl Three-dimensional micropatterning of bioactive hydrogels via two-photon laser scanning photolithography for guided 3D cell migration. Biomaterials 2008; 29 (20): 2962-68

11. Kolodziej Cm, Kim Sh, Broyer Rm, Saxer Ss, Decker Cg,Maynard Hd Combination of Integrin-Binding Peptide and Growth Factor Promotes

Cell Adhesion on Electron-Beam-Fabricated Patterns. J. Am. Chem. Soc. 2012; 134 (1): 247-55

12. Idota N, Tsukahara T, Sato K, Okano T,Kitamori T The use of electron beam lithographic graft-polymerization on thermoresponsive polymers for regulating the directionality of cell attachment and detachment. Biomaterials 2009; 30 (11): 2095-101

13. Mcusic Ac, Lamba Da,Reh Ta Guiding the morphogenesis of dissociated newborn mouse retinal cells and hES cell-derived retinal cells by soft lithography-patterned microchannel PLGA scaffolds. Biomaterials 2012; 33 (5): 1396-405

14. Cheng Cm,Leduc Pr Micropatterning polyvinyl alcohol as a biomimetic material through soft lithography with cell culture. Mol. Biosyst. 2006; 2 (6-7): 299-303

15. Arcaute K, Mann Bk,Wicker Rb Stereolithography of three-dimensional bioactive poly(ethylene glycol) constructs with encapsulated cells. Ann. Biomed. Eng. 2006; 34 (9): 1429-41

16. Chan V, Zorlutuna P, Jeong Jh, Kong H,Bashir R Three-dimensional photopatterning of hydrogels using stereolithography for long-term cell encapsulation. Lab Chip 2010; 10 (16): 2062-70

17. Hu W, Crouch As, Miller D, Aryal M,Luebke Kj Inhibited cell spreading on polystyrene nanopillars fabricated by nanoimprinting and in situ elongation. Nanotechnology 2010; 21 (38): 6

18. Hu W, Yim Ekf, Reano Rm, Leong Kw,Pang Sw Effects of nanoimprinted patterns in tissue-culture polystyrene on cell behavior. J. Vac. Sci. Technol. B 2005; 23 (6): 2984-89

19. O'meara Cm, Murray Jd, Mamo S, Gallagher E, Roche J,Lonergan P Gene silencing in bovine zygotes: siRNA transfection versus microinjection. Reprod. Fertil. Dev. 2011; 23 (4): 534-43

20. Xi Zy,Dobson Sl Characterization of Wolbachia transfection efficiency by using microinjection of embryonic cytoplasm and embryo homogenate. Appl. Environ. Microbiol. 2005; 71 (6): 3199-204

21. O'brien Ja,Lummis Scr Biolistic transfection of neuronal cultures using a hand-held gene gun. Nat. Protoc. 2006; 1 (2): 977-81

22. O'brien Ja, Holt M, Whiteside G, Lummis Scr,Hastings Mh Modifications to the hand-held Gene Gun: improvements for *in vitro* Biolistic transfection of organotypic neuronal tissue. J. Neurosci. Methods 2001; 112 (1): 57-64

23. Yalvac Me, Ramazanoglu M, Gumru Oz, Sahin F, Palotas A,Rizvanov Aa Comparison and Optimisation of Transfection of Human Dental Follicle Cells, a Novel Source of Stem Cells, with Different Chemical Methods and Electro-poration. Neurochem. Res. 2009; 34 (7): 1272-77

24. Byrnes Ck, Malone Rw, Akhter N, Nass Ph, Wetterwald A, Cecchini Mg, Duncan Md,Harmon Jw Electroporation enhances transfection efficiency in murine cutaneous wounds. Wound Repair Regen. 2004; 12 (4): 397-403

25. Baumgart J, Humbert L, Boulais E, Lachaine R, Lebrun Jj,Meunier M Off-resonance plasmonic enhanced femtosecond laser optoporation and transfection of cancer cells. Biomaterials 2012; 33 (7): 2345-50

26. Chakravarty P, Qian W, El-Sayed Ma,Prausnitz Mr Delivery of molecules into cells using carbon nanoparticles activated by femtosecond laser pulses. Nat. Nanotechnol. 2010; 5 (8): 607-11

27. Andersson As, Backhed F, Von Euler A, Richter-Dahlfors A, Sutherland D,Kasemo B Nanoscale features influence epithelial cell morphology and cytokine production. Biomaterials 2003; 24 (20): 3427-36

28. Anselme K, Ponche A,Bigerelle M Relative influence of surface topography and surface chemistry on cell response to bone implant materials. Part 2: biological aspects. Proc. Inst. Mech. Eng. Part H-J. Eng. Med. 2010; 224 (H12): 1487-507

29. Falconnet D, Csucs G, Grandin Hm,Textor M Surface engineering approaches to micropattern surfaces for cell-based assays. Biomaterials 2006; 27 (16): 3044-63

30. Sun K, Xie Yy, Ye Dk, Zhao Yy, Cui Y, Long F, Zhang W,Jiang Xy Mussel-Inspired Anchoring for Patterning Cells Using Polydopamine. Langmuir 2012; 28 (4): 2131-36

31. Yim Ekf, Reano Rm, Pang Sw, Yee Af, Chen Cs,Leong Kw Nanopattern-induced changes in morphology and motility of smooth muscle cells. Biomaterials 2005; 26 (26): 5405-13

32. Dalby Mj, Yarwood Sj, Riehle Mo, Johnstone Hjh, Affrossman S,Curtsi Asg Increasing fibroblast response to materials using nanotopography: morphological and genetic measurements of cell response to 13-nm-high polymer demixed islands. Exp. Cell Res. 2002; 276 (1): 1-9

33. Baac Hw, Lee Jh, Seo Jm, Park Th, Chung H, Lee Sd,Kim Sj Submicron-scale topographical control of cell growth using holographic surface relief grating. Mater. Sci. Eng. C-Biomimetic Supramol. Syst. 2004; 24 (1-2): 209-12

34. Choi Ch, Hagvall Sh, Wu Bm, Dunn Jcy, Beygui Re,Kim Cj Cell interaction with three-dimensional sharp-tip nanotopography. Biomaterials 2007; 28 (9): 1672-79

35. Kapoor A, Caporali Ehg, Kenis Pja,Stewart Mc Microtopographically patterned surfaces promote the alignment of tenocytes and extracellular collagen. Acta Biomater. 2010; 6 (7): 2580-89

36. Martinez Ec, Hernandez Jcr, Machado M, Mano Jf, Ribelles Jlg, Pradas Mm,Sanchez Ms Human Chondrocyte Morphology, Its Dedifferentiation, and Fibronectin Conformation on Different PLLA Microtopographies. Tissue Eng. Part A 2008; 14 (10): 1751-62

37. Dalby Mj, Giannaras D, Riehle Mo, Gadegaard N, Affrossman S,Curtis Asg Rapid fibroblast adhesion to 27 nm high polymer demixed nano-topography. Biomaterials 2004; 25 (1): 77-83

38. Dalby Mj, Gadegaard N, Tare R, Andar A, Riehle Mo, Herzyk P, Wilkinson Cdw,Oreffo Roc The control of human mesenchymal cell differentiation using nanoscale symmetry and disorder. Nat. Mater. 2007; 6 (12): 997-1003

39. Oh S, Brammer Ks, Li Ysj, Teng D, Engler Aj, Chien S,Jin S Stem cell fate dictated solely by altered nanotube dimension. Proc. Natl. Acad. Sci. U. S. A. 2009; 106 (7): 2130-35

40. Bettinger Cj, Langer R,Borenstein Jt Engineering Substrate Topography at the Micro- and Nanoscale to Control Cell Function. Angew. Chem.-Int. Edit. 2009; 48 (30): 5406-15

41. Christopherson Gt, Song H,Mao Hq The influence of fiber diameter of electrospun substrates on neural stem cell differentiation and proliferation. Biomaterials 2009; 30 (4): 556-64

42. Yang F, Murugan R, Ramakrishna S, Wang X, Ma Yx,Wang S Fabrication of nano-structured porous PLLA scaffold intended for nerve tissue engineering. Biomaterials 2004; 25 (10): 1891-900

43. Holmes Tc, De Lacalle S, Su X, Liu Gs, Rich A,Zhang Sg Extensive neurite outgrowth and active synapse formation on self-assembling peptide scaffolds. Proc. Natl. Acad. Sci. U. S. A. 2000; 97 (12): 6728-33

44. Srikanth M,Kessler Ja Nanotechnology-novel therapeutics for CNS disorders. Nat. Rev. Neurol. 2012; 8 (6): 307-18

45. Loesberg Wa, Te Riet J, Van Delft F, Schon P, Figdor Cg, Speller S, Van Loon J, Walboomers Xf,Jansen Ja The threshold at which substrate nanogroove dimensions may influence fibroblast alignment and adhesion. Biomaterials 2007; 28 (27): 3944-51

46. Altomare L, Gadegaard N, Visai L, Tanzi Mc,Fare S Biodegradable microgrooved polymeric surfaces obtained by photolithography for skeletal muscle cell orientation and myotube development. Acta Biomater. 2010; 6 (6): 1948-57

47. Engler Aj, Sen S, Sweeney Hl,Discher De Matrix elasticity directs stem cell lineage specification. Cell 2006; 126 (4): 677-89

48. Discher De, Janmey P,Wang Yl Tissue cells feel and respond to the stiffness of their substrate. Science 2005; 310 (5751): 1139-43

49. Bershadsky Ad, Balaban Nq,Geiger B Adhesion-dependent cell mechanosensitivity. Annu. Rev. Cell Dev. Biol. 2003; 19 677-95

50. Cukierman E, Pankov R, Stevens Dr,Yamada Km Taking cell-matrix adhesions to the third dimension. Science 2001; 294 (5547): 1708-12

51. Lo Cm, Wang Hb, Dembo M,Wang Yl Cell movement is guided by the rigidity of the substrate. Biophys. J. 2000; 79 (1): 144-52

52. Engler A, Bacakova L, Newman C, Hategan A, Griffin M,Discher D Substrate compliance versus ligand density in cell on gel responses. Biophys. J. 2004; 86 (1): 617-28

53. Discher De, Janmey P,Wang Y-L Tissue Cells Feel and Respond to the Stiffness of Their Substrate. Science 2005; 310 (5751): 1139-43

54. Sun M, Armstrong Sj, Kingham Pj, Terenghi G,Downes S Growth of NG108-15 cells and schwann cells on solvent cast PCL films. Tissue Eng. 2007; 13 (7): 1702-03

55. Suh Sw, Shin Jy, Kim Jh, Kim Jg, Beak Ch, Kim Di, Kim Sj, Jeon Ss,Choo Iw Effect of different particles on cell proliferation in polymer scaffolds using a solvent-casting and particulate leaching technique. Asaio J. 2002; 48 (5): 460-64

56. Chen Wc, Zhou Hz, Tang Mh, Weir Md, Bao Cy,Xu Hhk Gas-Foaming Calcium Phosphate Cement Scaffold Encapsulating Human Umbilical Cord Stem Cells. Tissue Eng. Part A 2012; 18 (7-8): 816-27

57. Montjovent Mo, Mathieu L, Hinz B, Applegate Ll, Bourban Pe, Zambelli Py, Manson Ja,Pioletti Dp Biocompatibility of bioresorbable poly(L-lactic acid) composite scaffolds obtained by supercritical gas foaming with human fetal bone cells. Tissue Eng. 2005; 11 (11-12): 1640-49

58. Townsend-Nicholson A,Jayasinghe Sn Cell electrospinning: a unique biotechnique for encapsulating living organisms for generating active biological microthreads/scaffolds. Biomacromolecules 2006; 7 (12): 3364-69

59. Lee Is, Kwon Oh, Meng W,Kang Ik Nanofabrication of microbial polyester by electrospinning promotes cell attachment. Macromol. Res. 2004; 12 (4): 374-78

60. Schugens C, Maquet V, Grandfils C, Jerome R,Teyssie P Polylactide macroporous biodegradable implants for cell transplantation .2. Preparation of polylactide foams by liquid-liquid phase separation. J. Biomed. Mater. Res. 1996; 30 (4): 449-61

61. Leong Kf, Cheah Cm,Chua Ck Solid freeform fabrication of three-dimensional scaffolds for engineering replacement tissues and organs. Biomaterials 2003; 24 (13): 2363-78

62. Sachlos E, Reis N, Ainsley C, Derby B,Czernuszka Jt Novel collagen scaffolds with predefined internal morphology made by solid freeform fabrication. Biomaterials 2003; 24 (8): 1487-97

63. Mikos Ag, Sarakinos G, Leite Sm, Vacanti Jp,Langer R LAMINATED 3-DIMENSIONAL BIODEGRADABLE FOAMS FOR USE IN TISSUE ENGINEERING. Biomaterials 1993; 14 (5): 323-30

64. Hapala I Breaking the barrier: methods for reversible permeabilization of cellular membranes. Crit Rev Biotechnol 1997; 17 (2): 105-22

65. Tarwadi, Jazayeri Ja,Pouton Cw Evaluations of novel transfection reagents based on lipopeptide structure as potential gene delivery vehicles. J. Gene. Med. 2005; 7 (8): 1126-26

66. Clamme Jp, Krishnamoorthy G,Mely Y Intracellular dynamics of the gene delivery vehicle polyethylenimine during transfection: investigation by two-photon fluorescence correlation spectroscopy. Biochim. Biophys. Acta-Biomembr. 2003; 1617 (1-2): 52-61

67. Wang H, Murphy R, Taaffe D, Yin S, Xia L, Hauswirth Ww, Bance M, Robertson Gs,Wang J Efficient cochlear gene transfection in guinea-pigs with adeno-associated viral vectors by partial digestion of round window membrane. Gene Ther. 2012; 19 (3): 255-63

68. Nasimuzzaman M, Russell Dw,Persons Da Enhanced Production of Foamy Viral Vectors Using Modified Vector Component Plasmids Coupled with PEI Transfection. Mol. Ther. 2009; 17 S309-S09

69. Norton Pa,Pachuk Cj Methods for DNA introduction into mammalian cells. Gene Transfer and Expression in Mammalian Cells 2003; 265-77

70. Baumgart J, Bintig W, Ngezahayo A, Willenbrock S, Murua Escobar H, Ertmer W, Lubatschowski H,Heisterkamp A Quantified femtosecond laser based opto-perforation of living GFSHR-17 and MTH53 a cells. Opt. Express 2008; 16 (5): 3021-31

71. Peng C, Palazzo Re,& Wilke Laser intensity dependence of femtosecond near-infrared optoinjection. Physical Review 2007; 041903

72. Stevenson Dj, Gunn-Moore Fj, Campbell P,Dholakia K Single cell optical transfection. Journal of The Royal Society Interface 2010; 7 (47): 863-71

73. Stracke F, Rieman I,Konig K Optical nanoinjection of macromolecules into vital cells. Journal of Photochemistry and Photobiology B: Biology 2005; 81 (3): 136-42

74. Tirlapur Uk,Konig K Cell biology - Targeted transfection by femtosecond laser. Nature 2002; 418 (6895): 290-91

75. Uchugonova A, Konig K, Bueckle R, Isemann A,Tempea G Targeted transfection of stem cells with sub-20 femtosecond laser pulses. Opt. Express 2008; 16 (13): 9357-64

76. Vikram K, Jason Pa,Abdulhakem Ye Reversible permeabilization using high-intensity femtosecond laser pulses: Applications to biopreservation. Biotechnology and Bioengineering 2005; 92 (7): 889-99

77. Lei M, Xu H, Yang H,Yao B Femtosecond laser-assisted microinjection into living neurons. Journal of Neuroscience Methods 2008; 174 (2): 215-18

78. Tirlapur Uk,Konig K Femtosecond near-infrared laser pulses as a versatile non-invasive tool for intra-tissue nanoprocessing in plants without compromising viability. Plant J. 2002; 31 (3): 365-74

79. Tirlapur Uk,Konig K Cell biology: Targeted transfection by femtosecond laser. Nature 2002; 418 (6895): 290-91

80. Stevenson D, Agate B, Tsampoula X, Fischer P, Brown Cta, Sibbett W, Riches A, Gunn-Moore F,Dholakia K Femtosecond optical transfection of cells: viability and efficiency. Opt. Express 2006; 14 (16): 7125-33

81. Uchugonova A, Konig K, Bueckle R, Isemann A,Tempea G Targeted transfection of stem cells with sub-20 femtosecond laser pulses. Opt. Express 2008; 16 (13): 9357-64

82. Davis Km, Miura K, Sugimoto N,Hirao K Writing waveguides in glass with a femtosecond laser. Opt. Lett. 1996; 21 (21): 1729-31

83. Assion A, Baumert T, Bergt M, Brixner T, Kiefer B, Seyfried V, Strehle M,Gerber G Control of chemical reactions by feedback-optimized phase-shaped femtosecond laser pulses. Science 1998; 282 (5390): 919-22

84. Chichkov Bn, Momma C, Nolte S, Vonalvensleben F,Tunnermann A Femtosecond, picosecond and nanosecond laser ablation of solids. Appl. Phys. A-Mater. Sci. Process. 1996; 63 (2): 109-15

85. Stuart Bc, Feit Md, Herman S, Rubenchik Am, Shore Bw,Perry Md Nanosecond-to-femtosecond laser-induced breakdown in dielectrics. Phys. Rev. B 1996; 53 (4): 1749-61

86. Schaffer Cb, Brodeur A, Garcia Jf,Mazur E Micromachining bulk glass by use of femtosecond laser pulses with nanojoule energy. Opt. Lett. 2001; 26 (2): 93-95

87. Supatto W, Debarre D, Moulia B, Brouzes E, Martin Jl, Farge E,Beaurepaire E *In vivo* modulation of morphogenetic movements in

Drosophila embryos with femtosecond laser pulses. Proc. Natl. Acad. Sci. U. S. A. 2005; 102 (4): 1047-52

88. Watanabe W, Arakawa N, Matsunaga S, Higashi T, Fukui K, Isobe K,Itoh K Femtosecond laser disruption of subcellular organelles in a living cell. Optics Express 2004; 12 (18): 4203-13

89. Ben-Yakar A,Byer Rl Femtosecond laser ablation properties of borosilicate glass. J. Appl. Phys. 2004; 96 (9): 5316-23

90. Braun A, Korn G, Liu X, Du D, Squier J,Mourou G SELF-CHANNELING OF HIGH-PEAK-POWER FEMTOSECOND LASER-PULSES IN AIR. Opt. Lett. 1995; 20 (1): 73-75

91. Kumagai H, Midorikawa K, Toyoda K, Nakamura S, Okamoto T,Obara M ABLATION OF POLYMER-FILMS BY A FEMTOSECOND HIGH-PEAK-POWER TI SAPPHIRE LASER AT 798-NM. Appl. Phys. Lett. 1994; 65 (14): 1850-52

92. Vogel A, Noack J, Hüttman G,Paltauf G Mechanisms of femtosecond laser nanosurgery of cells and tissues. Applied Physics B: Lasers and Optics 2005; 81 (8): 1015-47

93. Born M,Wolf E Principles of Optics: Electromagnetic Theory of Propagation, Interference and Diffraction of Light 1970; 440.

94. Grill S,Stelzer Ehk Method to calculate lateral and axial gain factors of optical setups with a large solid angle. J. Opt. Soc. Am. A 1999; 16 (11): 2658-65

95. Butler Jp, Tolić-Nørrelykke Im, Fabry B,Fredberg Jj Traction fields, moments, and strain energy that cells exert on their surroundings. American Journal of Physiology - Cell Physiology 2002; 282 (3): C595-C605

96. Dembo M,Wang Y-L Stresses at the Cell-to-Substrate Interface during Locomotion of Fibroblasts. Biophysical journal 1999; 76 (4): 2307-16

97. Khademhosseini A,Langer R Microengineered hydrogels for tissue engineering. Biomaterials 2007; 28 (34): 5087-92

98. Janmey Pa, Winer Jp, Murray Me,Wen Q The hard life of soft cells. Cell Motility and the Cytoskeleton 2009; 66 (8): 597-605

99. Pelham Rj, Wang Y-L Cell locomotion and focal adhesions are regulated by substrate flexibility. Proceedings of the National Academy of Sciences 1997; 94 (25): 13661-65

100. Lo C-M, Wang H-B, Dembo M,Wang Y-L Cell Movement Is Guided by the Rigidity of the Substrate. Biophysical journal 2000; 79 (1): 144-52

101. Paszek Mj, Zahir N, Johnson Kr, Lakins Jn, Rozenberg Gi, Gefen A, Reinhart-King Ca, Margulies Ss, Dembo M, Boettiger D, Hammer Da,Weaver Vm Tensional homeostasis and the malignant phenotype. Cancer Cell 2005; 8 (3): 241-54

102. Huebsch N, Arany Pr, Mao As, Shvartsman D, Ali Oa, Bencherif Sa, Rivera-Feliciano J,Mooney Dj Harnessing traction-mediated manipulation of the cell/matrix interface to control stem-cell fate. Nat Mater 2010; 9 (6): 518-26

103. Williams Jl,Lewis Jl Properties and an anisotropic model of cancellous bone from the proximal tibial epiphysis. J. Biomech. Eng.–T. ASME 1982; 104 (1): 50-56

104. Keskar Nr,Chelikowsky Jr Negative Poisson ratios in crystalline SiO2 from first-principles calculations. Nature 1992; 358 (6383): 222-24

105. Baughman Rh, Shacklette Jm, Zakhidov Aa,Stafstrom S Negative Poisson's ratios as a common feature of cubic metals. Nature 1998; 392 (6674): 362-65

106. Gunton Dj,Saunders Ga Young's modulus and Poisson's ratio of arsenic, antimony and bismuth. J. Mater. Sci. 1972; 7 (9): 1061

107. Baughman Rh,Galvao Ds Crystalline networks with unusual predicted mechanical and thermal properties. Nature 1993; 365 (6448): 735-37

108. Gardner Gb, Venkataraman D, Moore Js,Lee S Spontaneous assembly of a hinged coordination network. Nature 1995; 374 (6525): 792-95

109. Hall Lj, Coluci Vr, Galvao Ds, Kozlov Me, Zhang M, Dantas So,Baughman Rh Sign change of Poisson's ratio for carbon nanotube sheets. Science 2008; 320 (5875): 504-07

110. Lakes R Foam structures with a negative Poissons ratio. Science 1987; 235 (4792): 1038-40

111. Choi Jb,Lakes Rs Nonlinear properties of metallic cellular materials with a negative Poisson's ratio. J. Mater. Sci. 1992; 27 (19): 5375-81

112. Choi Jb,Lakes Rs Nonlinear properties of polymer cellular materials with a negative Poisson's ratio. J. Mater. Sci. 1992; 27 (17): 4678-84

113. Milton Gw Composite materials with Poisson's ratios close to -1. J. Mech. Phys. Solids 1992; 40 (5): 1105-37

114. Alderson Kl,Evans Ke The fabrication of microporous polyethylene having a negative Poisson's ratio. Polymer 1992; 33 (20): 4435-38

115. Caddock Bd,Evans Ke Microporous materials with negative Poisson's ratios. 1. Microstructure and mechanical properties. J. Phys. D Appl. Phys. 1989; 22 (12): 1877-82

116. Evans Ke,Caddock Bd Microporous materials with negative Poisson's ratios. 2. Mechanisms and interpretation. J. Phys. D Appl. Phys. 1989; 22 (12): 1883-87

117. Baughman Rh, Dantas So, StafstroM S, Zakhidov Aa, Mitchell Tb,Dubin Dhe Negative Poisson's ratios for extreme states of matter. Science 2000; 288 (5473): 2018-22

118. Lakes R Materials science: deformations in extreme matter. Science 2000; 288 (5473): 1976-77

119. Evans Ke,Alderson A Auxetic materials: functional materials and structures from lateral thinking. Adv. Mater. 2000; 12 (9): 617-28

120. Lakes R No contractile obligations. Nature 1992; 358 (6389): 713-14

121. Burns S Negative Poisson's ratio materials. Science 1987; 238 (4826): 551

122. Baughman Rh, Stafstram S, Cui C,Dantas So Materials with negative compressibilities in one or more dimensions. Science 1998; 279 (5356): 1522-24

123. Evans Ke, Nkansah Ma, Hutchinson Ij,Rogers Sc Molecular network design. Nature 1991; 353 (6340): 124-24

124. Rothenburg L, Berlin Ai,Bathurst Rj Microstructure of isotropic materials with negative Poisson's ratio. Nature 1991; 354 (6353): 470-72

125. Choi Jb,Lakes Rs Nonlinear-analysis of the Poisson's ratio of negative Poisson's ratio foams. J. Compos. Mater. 1995; 29 (1): 113-28

126. Gibson Lj, Ashby Mf, Schajer Gs,Robertson Ci The mechanics of two-dimensional cellular materials. P. Roy. Soc. Lond. A Mat. 1982; 382 (1782): 25-42

127. Almgren Rf An isotropic three-dimensional structure with Poisson's ratio = −1. J. Elast. 1985; 15 (4): 427-30

128. Chen Xg,Brodland Gw Mechanical determinants of epithelium thickness in early-stage embryos. J. Mech. Behav. Biomed. Mater. 2009; 2 (5): 494-501

129. Timmins Lh, Wu Qf, Yeh At, Moore Je,Greenwald Se Structural inhomogeneity and fiber orientation in the inner arterial media. Am. J. Physiol.–Heart C. 2010; 298 (5): H1537-H45

130. Burriesci G,Bergamasco G Annuloplasty prosthesis with an auxetic structure. 2007; (20070162112):

131. Lin Cy, Kikuchi N,Hollister Sj A novel method for biomaterial scaffold internal architecture design to match bone elastic properties with desired porosity. J. Biomech. 2004; 37 (5): 623-36

132. Lakes R Materials science: A broader view of membranes. Nature 2001; 414 (6863): 503-04

133. Jackman Rj, Brittain St, Adams A, Prentiss Mg,Whitesides Gm Design and fabrication of topologically complex, three-dimensional microstructures. Science 1998; 280 (5372): 2089-91

134. Veronda Dr,Westmann Ra Mechanical characterization of skin - finite deformations. J. Biomech. 1970; 3 (1): 111-22, IN9, 23-24

135. Soman P, Fozdar Dy, Lee Jw, Phadke A, Varghese S,Chen S A three-dimensional polymer scaffolding material exhibiting a zero Poisson's ratio. Soft Matter 2012; 8 (18): 4946-51

136. Soman P, Lee Jw, Phadke A, Varghese S,Chen S Spatial tuning of negative and positive Poisson's ratio in a multi-layer scaffold. Acta Biomaterialia 2012; 8 (7): 2587-94

137. Fozdar Dy, Soman P, Lee Jw, Han L-H,Chen S Three-Dimensional Polymer Constructs Exhibiting a Tunable Negative Poisson's Ratio. Advanced Functional Materials 2011; 21 (14): 2712-20

138. Masters Ig,Evans Ke Models for the elastic deformation of honeycombs. Compos. Struct. 1996; 35 (4): 403-22

139. Lee Ky,Mooney Dj Hydrogels for Tissue Engineering. Chemical Reviews 2001; 101 (7): 1869-80

140. Gibson Lj,Ashby Mf Cellular solids: structure and properties. Cambridge solid state science series 1997; 510

141. Fujiwara T, Bandi M, Nitta M, Ivanova Ev, Bronson Rt,Pellman D Cytokinesis failure generating tetraploids promotes tumorigenesis in p53-null cells. Nature 2005; 437 (7061): 1043-47

142. Estey Mp, Di Ciano-Oliveira C, Froese Cd, Bejide Mt,Trimble Ws Distinct roles of septins in cytokinesis: SEPT9 mediates midbody abscission. The Journal of Cell Biology 2010; 191 (4): 741-49

143. Dean So, Rogers Sl, Stuurman N, Vale Rd,Spudich Ja Distinct pathways control recruitment and maintenance of myosin II at the cleavage furrow during cytokinesis. Proceedings of the National Academy of Sciences of the United States of America 2005; 102 (38): 13473-78

144. Straight Af, Field Cm,Mitchison Tj Anillin Binds Nonmuscle Myosin II and Regulates the Contractile Ring. Molecular Biology of the Cell 2005; 16 (1): 193-201

145. Alberts B, Johnson A, Lewis J, Raff M, Roberts K,Walter P Molecular Biology of the Cell. 2002;

146. Van Noorden Cj Imaging enzymes at work: metabolic mapping by enzyme histochemistry. J Histochem Cytochem 2010; 58 (6): 481-97

147. Braak H, Alafuzoff I, Arzberger T, Kretzschmar H,Del Tredici K Staging of Alzheimer disease-associated neurofibrillary pathology using paraffin sections and immunocytochemistry. Acta Neuropathol. 2006; 112 (4): 389-404

148. Hayashi K, Hayashi M, Jalkanen M, Firestone Jh, Trelstad Rl,Bernfield M IMMUNOCYTOCHEMISTRY OF CELL-SURFACE HEPARAN-SULFATE PROTEOGLYCAN IN MOUSE-TISSUES - A LIGHT AND ELECTRON-

MICROSCOPIC STUDY. J. Histochem. Cytochem. 1987; 35 (10): 1079-88

149. Koester Sk,Bolton We Intracellular markers. J Immunol Methods 2000; 243 (1-2): 99-106

150. Aihara H,Miyazaki J Gene transfer into muscle by electroporation *in vivo*. Nat. Biotechnol. 1998; 16 (9): 867-70

151. Huang L,Li S Liposomal gene delivery: A complex package. Nat. Biotechnol. 1997; 15 (7): 620-21

152. Landen Cn, Chavez-Reyes A, Bucana C, Schmandt R, Deavers Mt, Lopez-Berestein G,Sood Ak Therapeutic EphA2 gene targeting *in vivo* using neutral liposomal small interfering RNA delivery. Cancer Res. 2005; 65 (15): 6910-18

153. Sims Ce,Allbritton Nl Analysis of single mammalian cells on-chip. Lab Chip 2007; 7 (4): 423-40

154. Andersson H,Van Den Berg A Microtechnologies and nanotechnologies for single-cell analysis. Curr Opin Biotechnol 2004; 15 (1): 44-9

155. Rotsch C, Jacobson K,Radmacher M Dimensional and mechanical dynamics of active and stable edges in motile fibroblasts investigated by using atomic force microscopy. Proceedings of the National Academy of Sciences of the United States of America 1999; 96 (3): 921-26

156. Chou Sy, Krauss Pr,Renstrom Pj IMPRINT OF SUB-25 NM VIAS AND TRENCHES IN POLYMERS. Appl. Phys. Lett. 1995; 67 (21): 3114-16

157. Stewart Md, Johnson Sc, Sreenivasan Sv, Resnick Dj,Willson Cg Nanofabrication with step and flash imprint lithography. J. Microlithogr. Microfabr. Microsyst. 2005; 4 (1): 6

158. Bailey T, Choi Bj, Colburn M, Meissl M, Shaya S, Ekerdt Jg, Sreenivasan Sv,Willson Cg Step and flash imprint lithography: Template surface treatment and defect analysis. 2000; 3572-77

159. Scheer Hc, Schulz H, Hoffmann T,Torres Cms Problems of the nanoimprinting technique for nanometer scale pattern definition. J. Vac. Sci. Technol. B 1998; 16 (6): 3917-21

160. Guo Lj, Cheng X,Chou Cf Fabrication of size-controllable nanofluidic channels by nanoimprinting and its application for DNA stretching. Nano Lett. 2004; 4 (1): 69-73

161. Ko Sh, Park I, Pan H, Grigoropoulos Cp, Pisano Ap, Luscombe Ck,Frechet Jmj Direct nanoimprinting of metal nanoparticles for nanoscale electronics fabrication. Nano Lett. 2007; 7 (7): 1869-77

162. Bao Lr, Cheng X, Huang Xd, Guo Lj, Pang Sw,Yee Af Nanoimprinting over topography and multilayer three-dimensional printing. J. Vac. Sci. Technol. B 2002; 20 (6): 2881-86

163. Kim Sh, Lee Kd, Kim Jy, Kwon Mk,Park Sj Fabrication of photonic crystal structures on light emitting diodes by nanoimprint lithography. Nanotechnology 2007; 18 (5): 5

164. Dong B, Zhong Dy, Chi Lf,Fuchs H Patterning of conducting polymers based on a random copolymer strategy: Toward the facile fabrication of nanosensors exclusively based on polymers. Adv. Mater. 2005; 17 (22): 2736-+

165. Ahn Sw, Lee Kd, Kim Js, Kim Sh, Park Jd, Lee Sh,Yoon Pw Fabrication of a 50 nm half-pitch wire grid polarizer using nanoimprint lithography. Nanotechnology 2005; 16 (9): 1874-77

166. Konijn M, Alkaisi Mm,Blaikie Rj Nanoimprint lithography of sub-100 nm 3D structures. 2005; 653-58

167. Pfeiffer K, Fink M, Ahrens G, Gruetzner G, Reuther F, Seekamp J, Zankovych S, Torres Cms, Maximov I, Beck M, Graczyk M, Montelius L, Schulz H, Scheer Hc,Steingrueber F Polymer stamps for nanoimprinting. Microelectron. Eng. 2002; 61-2 393-98

168. Barbero Dr, Saifullah Msm, Hoffmann P, Mathieu Hj, Anderson D, Jones Gac, Welland Me,Steiner U High resolution nanoimprinting with a robust and reusable polymer mold. Adv. Funct. Mater. 2007; 17 (14): 2419-25

169. Kamins Ti, Ohlberg Daa, Williams Rs, Zhang W,Chou Sy Positioning of self-assembled, single-crystal, germanium islands by silicon nanoimprinting. Appl. Phys. Lett. 1999; 74 (12): 1773-75

170. Pina-Hernandez C, Fu Pf,Guo Lj Easy duplication of stamps using UV-cured fluoro-silsesquioxane for nanoimprint lithography. 2008; 2426-29

171. Khang Dy,Lee Hh Sub-100 nm patterning with an amorphous fluoropolymer mold. Langmuir 2004; 20 (6): 2445-48

172. Kawata S, Sun Hb, Tanaka T,Takada K Finer features for functional microdevices - Micromachines can be created with higher resolution using two-photon absorption. Nature 2001; 412 (6848): 697-98

173. Serbin J, Egbert A, Ostendorf A, Chichkov Bn, Houbertz R, Domann G, Schulz J, Cronauer C, Frohlich L,Popall M Femtosecond laser-induced two-photon polymerization of inorganic-organic hybrid materials for applications in photonics. Opt. Lett. 2003; 28 (5): 301-03

174. Xing Jf, Dong Xz, Chen Wq, Duan Xm, Takeyasu N, Tanaka T,Kawata S Improving spatial resolution of two-photon microfabrication by using photoinitiator with high initiating efficiency. Appl. Phys. Lett. 2007; 90 (13): 3

175. Murooka K, Hattori K,Iizuka O Initial results of a 50 kV electron beam writer EBM-4000 for a 90 nm node photomask. 2003; 2668-71

176. Tan Df, Li Y, Qi Fj, Yang H, Gong Qh, Dong Xz,Duan Xm Reduction in feature size of two-photon polymerization using SCR500. Appl. Phys. Lett. 2007; 90 (7): 3

177. Maruo S, Ikuta K,Korogi H Force-controllable, optically driven micromachines fabricated by single-step two-photon micro stereolithography. J. Microelectromech. Syst. 2003; 12 (5): 533-39

178. Teh Wh, Durig U, Drechsler U, Smith Cg,Guntherodt Hj Effect of low numerical-aperture femtosecond two-photon absorption on (SU-8) resist for ultrahigh-aspect-ratio microstereolithography. J. Appl. Phys. 2005; 97 (5): 11

179. Han Lh, Mapili G, Chen S,Roy K Projection microfabrication of three-dimensional scaffolds for tissue engineering. J. Manuf. Sci. Eng.-Trans. ASME 2008; 130 (2): 4

180. Moon Jj, Hahn Ms, Kim I, Nsiah Ba,West Jl Micropatterning of Poly(Ethylene Glycol) Diacrylate Hydrogels with Biomolecules to Regulate and Guide Endothelial Morphogenesis. Tissue Eng. Part A 2009; 15 (3): 579-85

181. Curtis Asg, Gadegaard N, Dalby Mj, Riehle Mo, Wilkinson Cdw,Aitchison G Cells react to nanoscale order and symmetry in their surroundings. IEEE Trans. Nanobiosci. 2004; 3 (1): 61-65

182. Curtis A,Wilkinson C New depths in cell behaviour: reactions of cells to nanotopography. Cell Behaviour: Control and Mechanism of Motility 1999; 15-26

183. Curtis Asg, Casey B, Gallagher Jo, Pasqui D, Wood Ma,Wilkinson Cdw Substratum nanotopography and the adhesion of biological cells. Are symmetry or regularity of nanotopography important? Biophys. Chem. 2001; 94 (3): 275-83

184. Curtis Asg,Varde M CONTROL OF CELL BEHAVIOR - TOPOLOGICAL FACTORS. J. Natl. Cancer Inst. 1964; 33 (1): 15-&

185. Fozdar Dy, Zhang W, Palard M, Patrick C,Chen S Flash imprint lithography using a mask aligner: a method for printing nanostructures in photosensitive hydrogels. Nanotechnology 2008; 19 (21): 13

186. Mcdonald Jc, Duffy Dc, Anderson Jr, Chiu Dt, Wu Hk, Schueller Oja,Whitesides Gm Fabrication of microfluidic systems in poly(dimethylsiloxane). Electrophoresis 2000; 21 (1): 27-40

187. Rolland Jp, Van Dam Rm, Schorzman Da, Quake Sr,Desimone Jm Solvent-resistant photocurable "liquid teflon" for microfluidic device fabrication. J. Am. Chem. Soc. 2004; 126 (8): 2322-23

188. Rolland Jp, Hagberg Ec, Denison Gm, Carter Kr,De Simone Jm High-resolution soft lithography: Enabling materials for nanotechnologies. Angew. Chem.-Int. Edit. 2004; 43 (43): 5796-99

189. Mcbeath R, Pirone Dm, Nelson Cm, Bhadriraju K,Chen Cs Cell shape, cytoskeletal tension, and RhoA regulate stem cell lineage commitment. Dev. Cell 2004; 6 (4): 483-95

190. Adler Af,Leong Kw Emerging links between surface nanotechnology and endocytosis: Impact on nonviral gene delivery. Nano Today 2010; 5 (6): 553-69

191. Liu Cx, Yu Wy, Chen Zj, Zhang J,Zhang N Enhanced gene transfection efficiency in CD13-positive vascular endothelial cells with targeted poly(lactic acid)-poly(ethylene glycol) nanoparticles through caveolae-mediated endocytosis. J. Control. Release 2011; 151 (2): 162-75

192. Soenen Sj, Rivera-Gil P, Montenegro Jm, Parak Wj, De Smedt Sc,Braeckmans K Cellular toxicity of inorganic nanoparticles: Common aspects and guidelines for improved nanotoxicity evaluation. Nano Today 2011; 6 (5): 446-65

193. Adler Af, Speidel At, Christoforou N, Kolind K, Foss M,Leong Kw High-throughput screening of microscale pitted substrate topographies for enhanced nonviral transfection efficiency in primary human fibroblasts. Biomaterials 2011; 32 (14): 3611-19

194. Cell Biology's Open Cases. Science 2011; 334 (6059): 1051

195. Ho Yp, Grigsby Cl, Zhao F,Leong Kw Tuning Physical Properties of Nanocomplexes through Microfluidics-Assisted Confinement. Nano Lett. 2011; 11 (5): 2178-82